공학석사 학위논문

Fully vacuum–processed perovskite solar cells with high open circuit voltage using MoO_3/NPB layer

MoO_3/NPB 층을 사용한 높은 개방전압의 진공 공정으로 제작된 페로브스카이트 태양전지

2015년 2월

서울대학교 대학원

재료공학부

김 범 수

Fully vacuum–processed perovskite solar cells with high open circuit voltage using MoO_3/NPB layer

지도 교수 김 장 주

이 논문을 공학석사 학위논문으로 제출함

2015년 2월

서울대학교 대학원

재료공학부

김 범 수

김범수의 공학석사 학위논문을 인준함

2015년 2월

주 조 원 호 (인)

부 김 장 주 (인)

부 남 기 태 (인)

Abstract

Fully vacuum–processed perovskite solar cells with high open circuit voltage using MoO_3/NPB layer

Kim Beom-Soo

Department of Materials Science and Engineering

The Graduate School

Seoul National University

Recently, organic/inorganic hybrid (e.g. $CH_3NH_3PbI_3$, $CH_3NH_3PbI_{3-x}Cl_x$) perovskite based solar cells attract large attention because of the remarkably high power conversion efficiencies. Most of the devices reported up to now have been fabricated using solution processes. One of the critical issues of the solution processed perovskite solar cells is the reproducibility coming from the difficulties in controlling the uniformity, pin-hole formation, sensitivity to moisture and air of the perovskite film. Vacuum evaporation has a potential for high reproducibility and controllability due to solvent free processes combined with controllable growth parameters in a clean and inert environment. Nevertheless, the fully vacuum–processed perovskite solar cells have been rarely reported up to now. The other crucial issue

is the charge transport materials, mainly hole transport materials(HTM's), to enhance the device performance. The widely used HTM, 2,2',7,7'-Tetrakis(N,N-di-p-methoxyphenylamine)-9,9'-spirobifluorene (spiro-OMeTAD) is not an optimized HTM for the $CH_3NH_3PbI_3$ based solar cells, since spiro-OMeTAD possesses a few hundred meV higher HOMO level than valance band (VB) edge of $CH_3NH_3PbI_3$.

This thesis presents high efficiency perovskite solar cells with high open circuit voltage using full vacuum process employing molybdenum oxide (MoO_3) and N,N′-Di(1-naphthyl)-N,N′-diphenyl-(1,1′-biphenyl)-4,4′-diamine (NPB) as a new hole extraction layer. All the layers in the solar cells including the perovskite active layer, hole extraction layers and electron extraction layers were deposited in the vacuum process. Uniform crystalline perovskite layers were able to be grown on the NPB layer under optimized conditions. The grain size of the films were about 100 nm with the root mean square roughness of 9.7 nm. The solar cells employing the MoO_3/NPB as the hole extraction layer resulted in a high open circuit voltage (V_{OC}) of 1.12 V, which is one of the highest values reported up to now in perovskite solar cells. Due to the effective hole extraction and high V_{OC}, the devices showed a maximum power conversion efficiency (PCE) of 13.7% with J_{SC} of 18.1 mA/cm^2, V_{OC} of 1.12 V and *FF* of 0.68. It turned out missing one

of the MoO_3 or NPB layers resulted in much poor solar cell performance due to either the failure of the formation of ohmic contact with the ITO electrode (missing the MoO_3 layer) or due to the lack of the electron blocking layer or poor crystallinity of the perovskite layer (missing the NPB layer). The vacuum processed perovskite solar cells showed relatively high reproducibility showing the average value of PCE of 11.1%. The J_{SC} and V_{OC} are distributed within 17.2 mA/cm^2 ~ 19.5 mA/cm^2 and 0.98 V ~ 1.12 V respectively, exhibiting small deviation within approximately 7% from the average values. The *FF* values show a relatively wide distribution, 0.39~0.68, hence causing the similar distribution of PCE values, 7.1%~13.7%. Still the variation of the performance of the solar cells fabricated using the vacuum process is fairly narrow compared to the normal solution processed perovskite solar cells. Further study is required to find out the origin of the variation of *FF*, thereby to enhance the better reproducibility. The vacuum processed perovskite solar cells showed hysteresis depending on sweep direction. The device with MoO_3/NPB layer showed PCE of 12.1% with J_{SC} of 18.1 mA/cm^2, V_{OC} of 1.09 V and *FF* of 0.62 in the forward scan direction whereas overall solar cell parameter decreased in the reverse scan direction showing PCE of 10.3% with J_{SC} of 17.1 mA/cm^2, V_{OC} of 1.07 V and *FF* of 0.56. The origin of the hysteresis is important issue, however it has not been clearly figured out yet.

Keywords: Organic/inorganic hybrid perovskite solar cell, full vacuum-process, reproducibility, MoO_3, NPB,

Student Number: 2012 - 20577

List of Tables

List of Figures

Chapter 1
Introduction

1.1 Motivation and outline of thesis

1.1.1 Motivation

Recently, hybrid organic/inorganic perovskite (e.g., $CH_3NH_3PbI_3$) based solar cells attract large attention because of the remarkably high power conversion efficiencies (PCEs) combined with low temperature processes [1-5].

Most of the devices reported up to now have been fabricated using solution processes. One of the critical issues of the solution processed perovskite solar cells is the reproducibility coming from the difficulties in controlling the uniformity [6-7], pin-hole formation [7-8], sensitivity to moisture and air [9-10]. A variety of approaches have been introduced such as sequential deposition [2,8,11], solvent modifications [4,12-16], manipulation of the crystallization time [17,18], and changing the annealing conditions [19-22], which are mostly attempted in the modification of the solution processes. Vacuum evaporation has a potential for high reproducibility and controllability due to solvent free processes combined with controllable

growth parameters in a clean and inert environment. [3,23-25] Nevertheless, the fully vacuum–processed perovskite solar cells have been rarely reported up to now. Polander et al. recently reported fully vacuum–processed perovskite solar cells using various hole transporting layers (HTLs) and found that 2,2',7,7'-tetra(N,N -di-p -tolyl)amino-9,9-spirobifluorene (spiro-TTB) possessing HOMO level of -5.3 eV resulted in the higher solar cell performance with V_{OC} of 1.07 V and PCE of 10.9% than spiro-2',7,7'-tetrakis-(N,N-di-p-methoxyphenylamine)-9,9'-spirobifluorene (spiro-OMeTAD), possessing the HOMO level of -5.0 eV which showed V_{OC} of 0.85 V and PCE of 7.7%. [24] In addition, Shultz et al. identified that the mismatch between the HOMO level of the hole transport material (HTM) and the valence band (VB) edge of $CH_3NH_3PbI_3$ (-5.4 eV) is a crucial factor of lowering V_{OC}. [26]

Therefore, the widely used spiro-OMeTAD is not an optimized HTM for the $CH_3NH_3PbI_3$ based solar cells, since spiro-OMeTAD possesses a few hundred meV higher HOMO level than VB edge of $CH_3NH_3PbI_3$. Various attempts have been reported in order to find HTMs for minimizing the energetic loss in perovskite solar cells [27-32]. In the solution processes, however, the material selection of an upper layer (HTM) is restricted because under layers should not be dissolved by the solvent of the upper layer. Fully vacuum–processed perovskite solar cells are a promising solution to find the efficient hole extraction layers possessing the HOMO level of -5.4 eV with good reproducibility. In these regards, the fully vacuum–processed solar cells employing the hole extraction layers minimizing the energetic losses will be presented.

1.1.2 Outline of thesis

In chapter 1, the brief introduction of the development of the perovskite solar cell and the physical properties of the perovskite will be described. Also the general working mechanism of the perovskite solar cell and the fabrication methods for the perovskite films will be introduced.

In chapter 2, the detail methodology to fabricate the high quality perovskite films using the vacuum co-evaporation will be explained. The different materials, mixed halide perovskite ($CH_3NH_3PbI_{3-x}Cl_x$) and triiodie perovskite ($CH_3NH_3PbI_3$) in vacuum process were discussed. In addition the deposition condition and the effect on the film properties, especially the surface morphology, are investigated.

In chapter 3, the functions of the hole extraction layers, molybdenum oxide (MoO_3) and N,N′-Di(1-naphthyl)-N,N′-diphenyl-(1,1′-biphenyl)-4,4′-diamine (NPB) layers will be investigated. Also the application of these layers into the vacuum processed perovskite solar cells were demonstrated. The roles of the MoO_3 laye, forming an ohmic contact at the ITO/NPB interface, hence reducing the hole injection barrier and resulting in the built-in field in the device will be discussed. The function of the NPB layer playing the important roles as the electron blocking layer with its sufficiently lower lowest unoccupied molecular orbital (LUMO) level comparing to the conduction band of

$CH_3NH_3PbI_3$ will be described.

In chapter 4, the reproducibility of the vacuum processed perovskite solar cells will be discussed. The detail analyses depending on the solar cell parameters, such as JSC, VOC, FF and PCE were investigated. Also the batch to batch analyzation will be carried out.

In chapter 5, the hysteresis behavior of the fabricated perovskite solar cells and the plausible origins will be discussed. The hysteresis depending on the structures, with or without NPB or MoO_3 layers, will be discussed iin detail. Since the exact origin of this hysteresis is not clear yet, the previously suggested plausible origins will be discussed in this chapter.

1.2 Perovskite solar cells

1.2.1 Material properties of the perovskite

In perovskite solar cells, the perovskite usually composed with organic cat ion, metal, and halogen components thus it is called as organometal halide perovskite. $CH_3NH_3^+$, Pb^+, I^- are most widely used components as the organic cat ion, metal and halogen parts respectively in the orgaometal halide prvoskite, where a few papers report that $HC(NH_2)_2^+$[33, 34], Sn[35, 36] used perovskites. $CH_3NH_3^+$ plays the role of providing a charge balance in perovskite structure without

covalent interactions with other components where $Pb2_{+}$ and I^{-} are bonded with the combination of covalent and ionic bonds [37]. In this perovskite structure, the lower part of the conduction band (CB) is mainly composed by hybridization of *s* orbital of Pb and *p* orbital of I where upper part of the valance band (VB) is mainly comprised of *p* orbital of Pb [37]. With this characteristic, $CH_3NH_3PbI_3$ shows the optical band gap of 1.5 eV and exhibits high absorption coefficients in the visible light range [38]. In addition, it has been reported that the diffusion lengths of electron and hole are up to 1 micrometer [39]. The one of the crucial reasons for this long electron-hole diffusion lengths is that the dominant point defects, such as Iodine interstitial defects, Methylammonium interstitial defects, Iodine vacancies generate shallow traps against CB or VB [37]. Therefore, it is possible to diffuse over a micrometer for the electrons and holes through the CB and VB respectively. Additionally, it has been reported that $CH_3NH_3PbI_3$ possesses inherently benign grain boundaries, which may act as traps in the film [37]. With these characteristics, the high absorption coefficients combined with long electron-hole diffusion lengths attributed from the shallow taps of the point defects and benign grain boundaries, $CH_3NH_3PbI_3$ generates the charge carriers then transports the carriers to the electron or hole transport layers under the lights. These properties are suitable for the active layer in the photovoltaic devices.

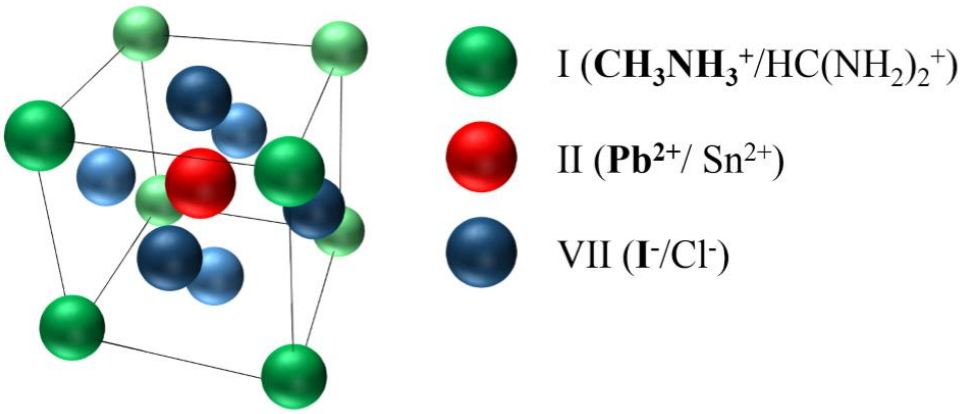

Figure. 1.1 The structure of organometal halide perovskite. The most widely used components are marked with bold in the parentheses which are $CH_3NH_3^+$, Pb^{2+}, I^- for the monovalent organic cat ion, divalent metal and the halogen components respectively.

1.2.2 Working principles of the perovskite solar cells

In the perovskite solar cells, it was debatable whether the exciton or free carriers are dominantly generated since the exciton binding energy is know to be about 50 meV [40] which results in delocalized Wannier-like exciton characteristics. However, recently V. D'Innocenzo et al. reported that the free carriers are dominantly generated at room temperature in the $CH_3NH_3PbI_3$ calculated by thermodynamic based numerical simulation [41]. Therefore, in perovskite solar cells the free carriers are mainly considered.

Additionally, A. Marchioro et al. identified the charge transfer processes in the lead iodide perovskite solar cells using a transient absorption spectroscopy [42]. As mentioned above, after the free carriers are generated, the carriers in the perovskite layer diffuse to the charge transport layers then the carriers are collected at the selective electrodes. Also, Marchioro et al. argued that there are certain amounts of the back charge transfer, electron transfer from electron transport layer (ETL) to the perovskite and hole transfer from the hole transport layer (HTL) to the perovskite respectively, in the perovskite solar cells.

1.2.3 Charge extraction layers in perovskite solar cells

There are two main roles for the charge extraction layers in the

perovskite solar cells. The first function is forming a selective contact of electron and holes against to the electrodes. Since the free carriers are generated in the bulk of the perovskite, the free carriers can diffuse to either direction to the anode or cathode. Therefore, the HTM might act as an electron blocking layer while the ETM might act as a hole blocking layer. In order to act as the blocking layers selectively, the energy levels should be considered for the each layer. For example, since the CB of the $CH_3NH_3PbI_3$ is -3.9 eV, the CB or the lowest unoccupied molecular orbital (LUMO) level of the HTM should be lower than -3.9 eV to prevent electron transfer through the HTM, at the same time the VB edge or highest occupied molecular orbital (HOMO) level should be lower than -5.4 eV since the CB of the perovskite is -5.4 eV. Likewise, the ETM should possesses the VB edge or HOMO level of higher than -5.4 eV to prevent hole transfer through the ETM and the CB or LUMO level should be higher than -3.9 eV to transfer the electrons from the perovskite layer.

The charge extraction layers also affects to the open circuit voltage [43]. If the CB or LUMO level of the ETM is closed to the CB of the perovskite, or the VB edge or HOMO level of the HTM is closed to the VB edge of the perovskite the built in field hence the open circuit voltage can be increased, in the assumption of the ohmic contact is formed between the charge transport materials and the electrodes, since the open circuit voltage, which is expressed by following equation.

$$V_{OC}=E_{HOMO(VB)\ of\ HTM}-E_{LUMO(CB)\ of\ ETM}\fallingdotseq \Phi_{anode}-\Phi_{cathode} \quad (1)$$

Therefore, to maximize the open circuit voltage of the perovskite solar cells, matching the CB of the perovskite to the CB or LUMO level of the ETM and VB of the perovskite to the VB edge or HOMO level of the HTM would be a good strategy.

1.2.4 Methodes to fabricate the perovskite films

$CH_3NH_3PbI_3$ is formed via the reaction between CH_3NH_3I (Methylammonium Iodide, MAI) and PbI_2 (Lead Iodide). There are several methods to fabricate this materials as follows.

Spin coating

The spin coating is carried out by the casting the mixed solvent containing MAI and PbI_2 on to the desired substrates. In this process, the solvent should be resolving both CH_3NH_3I and PbI_2 and the widely used solvents is dimethylformamide (DMF). In the mixed solvent of the MAI and PbI_2, the perovskite forms in a very short time once the solvent drops onto the substrates with quickly evaporating DMF. This is often indicated that it causes a poor morphologies since the crystallization form the mixed solvent occurs quickly therefore there would be a lot of voids in the film, which causes significant degrading

of the film quality and the device performance in the solar cells. To retard the crystallization, some methods such as a dropping toluene or use of dimethyl sulfoxide (DMSO) which evaporates slowly comparing to DMF [4,13].

Sequential deposition

In the sequential deposition, the PbI_2 layer is deposited on the substrate by spin-coating and PbI_2 deposited substrate is dipped into the MAI solution in the isopropyl alcohol (IPA) solvent. Burshka et al reported this method to fabricate the perovskite solar cell and the authors showed that the pin-hole free, compact perovskite film which resulted in the PCE of 15% [2]. The formation of the perovskite is possible since the MAI inter-diffuses into the PbI_2 layer, therefore the annealing process is necessary to form the perovskite structure.

Vacuum deposition

The vacuum deposition perovskite layer for the solar cell was reported by a few groups [3,23]. In this process, MAI and the lead halide (PbI_2 or $PbCl_2$) are co-evaporated in the vacuum chamber and the composition is controlled by the deposition rate of the each source. It is reported that the use of $PbCl_2$ requires the post annealing process to form the perovskite structure since the MAI should be supplied excessively to satisfy the stoichiometry, and this excessive MAI should

be removed whereas the iodide perovskite using PbI_2 can be formed without annealing processes.

Chapter 2

Vacuum deposition of $CH_3NH_3PbI_3$

2.1 Introduction

In the perovskite solar cells, the one of the critical issues, as mentioned in the chapter 1.1.1, is the reproducibility since the film formation is a difficult due to the characteristics of the perovskite films such as non-uniform surface, voids in the films, pin-hole formation and the sensitivity to the moisture. This factors cause significant problems in terms of the reproducibility when the film is applied to the photovoltaic devices. Therefore, to enhance the reproducibility in other words to enhance the film quality various attempts have been introduced such as the solvent modifications [4, 12-16], changing the annealing conditions [19-22]. The Vacuum process has a potential for high reproducibility and controllability due to solvent free process combined with controllable growth parameters in a clean and inert environment [3, 23-25]. In this chapter, the detail experiment method of the vacuum processed perovskite and its effect on the film characteristics will be discussed.

2.2 Behavior of CH_3NH_3I in the vacuum deposition

Fig. 2.1a shows the schematic description of the thermal evaporating materials and its evaporating trajectories. As shown in the figure, the vacuum gauge is at the side of the vacuum chamber which reads the vacuum pressure by the difference of the conductivity dependent on the surrounded molecules, typically the gaseous species such as nitrogen, oxygen, hydrogen and moistures. Therefore, the typical thermal evaporating materials does not cause the increase of the vacuum pressure since the ejected molecules from the source adsorb on the substrates or the any part of the chamber where the molecules are encountered, rather than exist in the chamber with the gaseous state in the chamber which might cause the increase of the vacuum pressure. However, as shown in Fig. 2.1b, when MAI is evaporated in the vacuum chamber, the MAI source are randomly distributed in the chamber behaves as gaseous species causing the increase of the vacuum pressure infiltrating to the vacuum gauge. This behavior might be caused from the low molecular weight of MAI (157 g/mol), low adsorption characteristic and low evaporating temperature (~150℃). With these characteristics when the MAI is only deposited onto the

glass substrate, it is difficult to measure the accurate thickness since the MAI is rarely adsorbed onto the substrate. Also, the gaseous like behavior of the MAI causes the contamination of the other sources in the vacuum chamber, the deposition process should be carried out with this consideration.

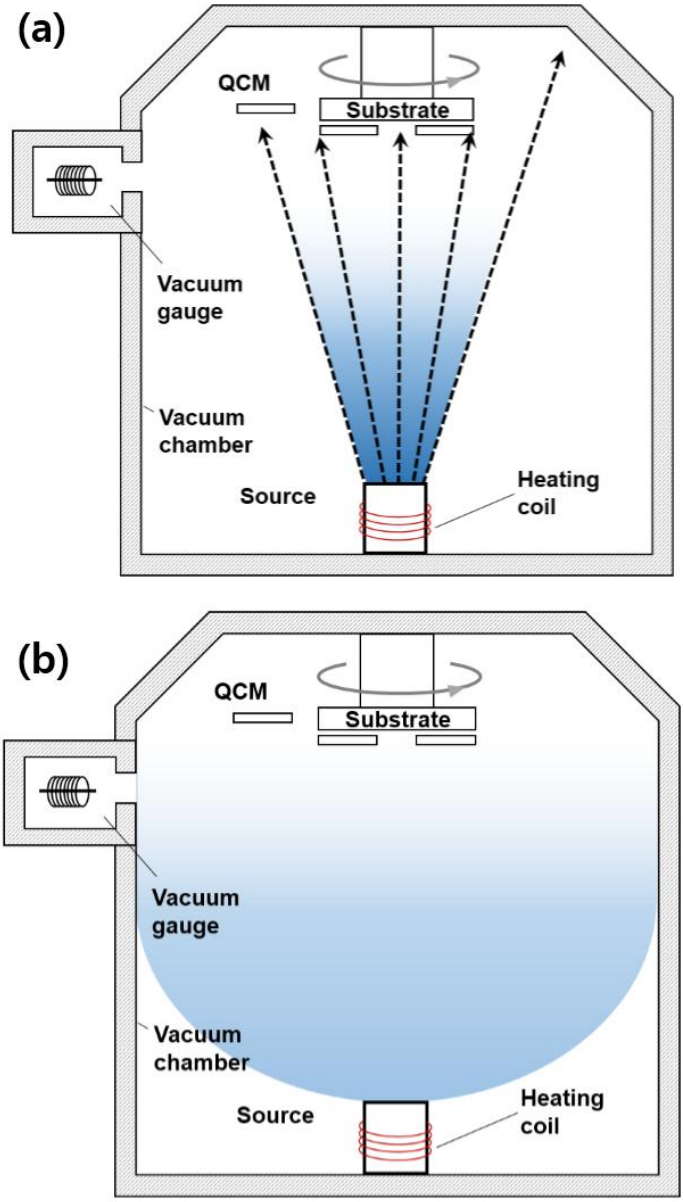

Figure 2.1. (a) The schematic description of behavior of the typical thermal evaporated materials. The dashed arrows indicate the trajectory of the evaporated materials from the source. (b) The schematic description of evaporated CH_3NH_3I (MAI) in the vacuum chamber. The round figure in presents the random distribution of the evaporated materials from the source.

2.3 Co-deposition with $PbCl_2$ ($CH_3NH_3PbI_{3-x}Cl_x$)

The mixed halide perovskite, which is typically formed with the reaction between MAI and $PbCl_2$, consequently forms the $MAPbI_{3-x}Cl_x$ is the widely used material next to $MAPbI_3$. In this mixed halide perovskite, the proportion of Cl is known to be less than 5% over iodine, which indicates the "x" in $MAPbI_{3-x}Cl_x$ is less than 0.15 [44]. Therefore, in order to satisfy the stoichiometry in the perovskite, the molar ratio of MAI:$PbCl_2$ should be approximately 3:1 which requires the excessive MA^+ and Cl^- components should be removed after the deposition. For the removal process, annealing the substrate at 150℃ is carried out [3].

The vacuum co-deposition of the mixed halide perovskite was carried out without the information of the deposition rate of the MAI, since the poor adsorption coefficient onto the substrate which makes the measuring the film thickness is difficult. In this experiment, the deposition rate of $PbCl_2$ was set to 0.5 Å/s which had been calibrated before the deposition using a profilometry (KLA-Tencor Alpha-Step IQ) where the deposition rate of MAI was 0.5 Å/s using the a random tooling factor, but maintained the deposition rate constant during the deposition. After the deposition, the substrate was annealed in the nitrogen ambient at 150℃. The fabricated perovskite film is shown in

Fig. 2.2 which exhibits the root mean square (RMS) value of the 34 nm and the maximum peak to valley value of 225 nm from the 320 nm of the perovskite film. Due to this film characteristics, when this film is applied to the perovskite solar cell the device was not performed appropriately showing the most of the devices in a short-circuit state, which assembly is resulted from the contact of the electrodes due to the rough surface and pin-holes.

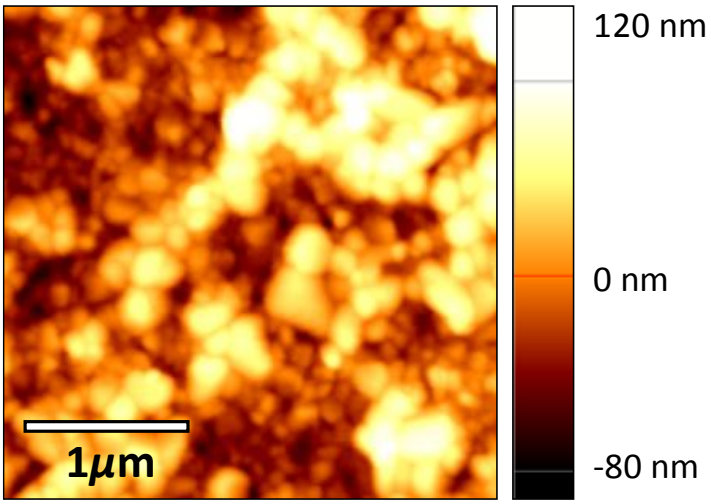

Figure 2.2 The atomic force microscope (AFM) image of the 320 nm thick mixed halide perovskite film grown on to the ITO substrate.

2.4 Co-deposition with PbI_2 ($CH_3NH_3PbI_3$)

The triiodide perovskite, $CH_3NH_3PbI_3$, is formed with the reaction between MAI and PbI_2. The molar ratio of MAI:PbI_2 is 1:1 to form $CH_3NH_3PbI_3$, therefore ideally it is not required to provide any excessive $CH_3NH_3^+$ ions whereas in mixed perovskite system the $CH_3NH_3^+$ ions are necessarily incorporated in the perovskite system as mentioned in chapter 2.3. Therefore, the annealing process to remove the excessive $CH_3NH_3^+$ including components is not required in the vacuum deposited $CH_3NH_3PbI_3$ perovskite. As shown in fig. 2.3, the quartz crystal microbalances 1 (QCM) was located on the PbI_2 source which reads only the deposition rate of PbI_2. The QCM 1 was enclosed by the aluminum foil to exclude the effect of the CH_3NH_3I, since its gas-like behavior in the vacuum chamber. In this process, firstly the deposition rate was PbI_2 was reached to the steady state. QCM 2 was located at the near the substrate which enables to read the deposition rate of CH_3NH_3I and also the thickness of the perovskite since it reads the both PbI_2 and CH_3NH_3I which forms the perovskite on the substrate. The base pressure of the vacuum chamber was about 1×10^{-6} Torr and this pressure was increased up to 2×10^{-5} Torr when CH_3NH_3I is deposited. Regardless this increase of the vacuum pressure, the deposition rates of the PbI_2 and CH_3NH_3I are maintained constant

during the co-deposition. To form the 320 nm thick of the perovskite, 150 nm thick of PbI_2 was deposited measured from the QCM 1 which took about 1 hour for the deposition.

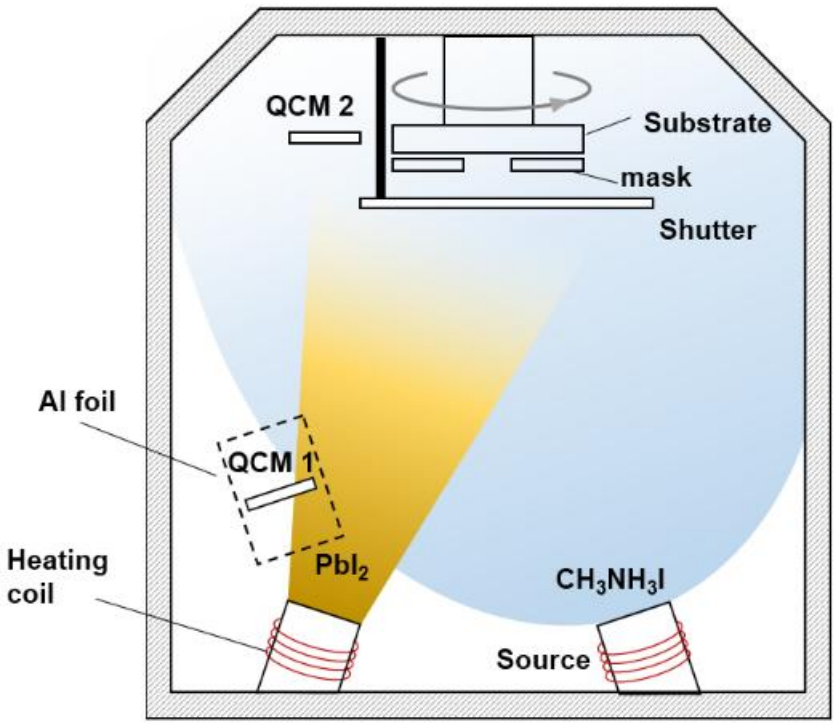

Figure 2.3. The schematic description co-evaporating the PbI_2 and CH_3NH_3I in the vacuum chamber.

2.5 Film characterization

2.5.1 Absorbance and XRD patterns

Fig. 2.5 shows the absrobance of a 320nm thick $CH_3NH_3PbI_3$ film grown on a glass substrate which were recorded by a VARIAN Cary 5000 UV–vis spectrophotometer. The absorbance corresponds to previously reported data in visible light range, which implies that the perovskite structure via vacuum co-evaporation described in the chapter 2.4 was successfully formed.

Fig 2.5 shows the XRD patterns of the fabricated $CH_3NH_3PbI_3$ film grown on a ITO (150 nm)/MoO_3 (5 nm)/NPB (20 nm) substrate. The peaks at 14.06˚, 28.26˚ 31.73˚, 40.55˚ and 43.13˚ correspond to (110), (220), (310), (224) and (314) planes of the tetragonal form of $CH_3NH_3PbI_3$ structure [34, 35]. It is worth noting that the high intensity of (110) and (220) peaks represent that the highly preferred oriented of the perovskite film on the NPB layer, which will be used as a HTM later. The preferred orientation, [110] direction, is demonstrated in Fig. 2.6.

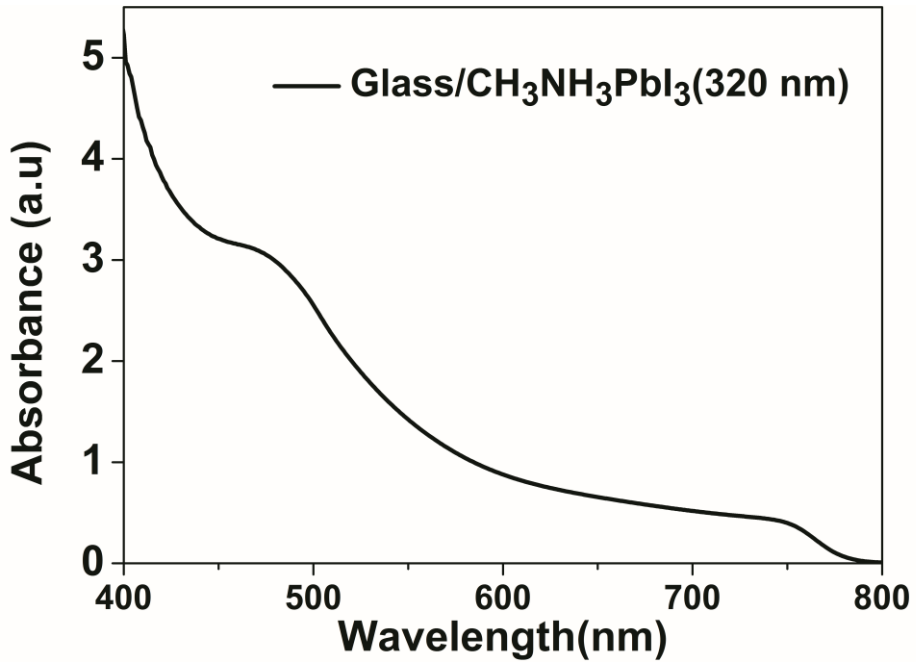

Figure 2.4 The absorbance of the 320 nm thick $CH_3NH_3PbI_3$ film grown on the glass substrate using vacuum co-evaporation.

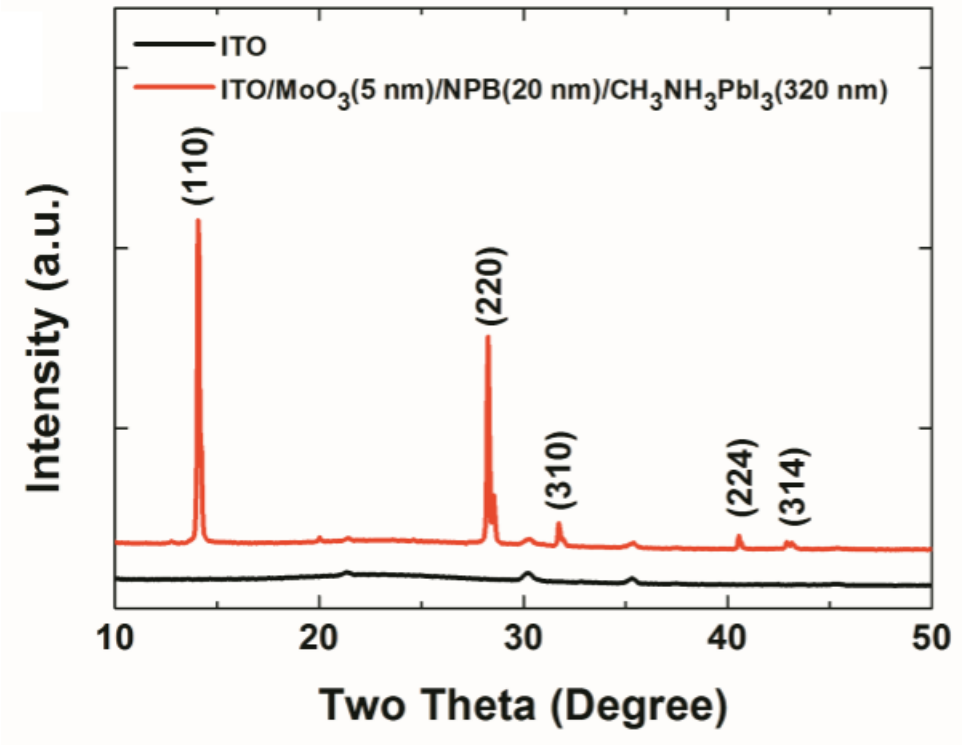

Figure 2.5 The X-ray diffraction (XRD) patterns of a 320 nm thick $CH_3NH_3PbI_3$ film grown on the ITO/MoO_3(5 nm)/NPB (20 nm) substrate using vacuum co-evaporation.

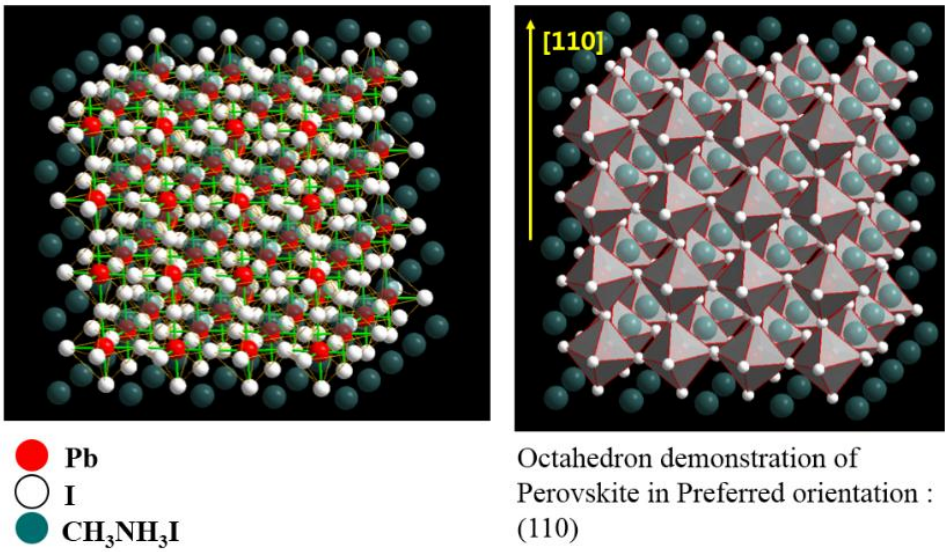

Figure 2.6. The demonstration of $CH_3NH_3PbI_3$ perovskite in the preferred orientation along (110) direction. This figure was drawn by Diamond 3.2 program.

2.5.2 Surface ananlyzes

Fig. 2.7 shows the atomic force miecroscopy (AFM) image of the $CH_3NH_3PbI_3$ perovskite film grown on ITO/MoO3 (5 nn)/NPB (20nm) substrate, which was taken by PSIA XE-100 scanning probe microscope in noncontact mode. The root mean squre (RMS) roughness is 9.7nm and the maximum peak to valley value is 70 nm from the 320 nm thick film. These values can be consiered small comparing to the previously fabricated film, in chapter 2.3. Also, Fig. 2.8. shows the red line profile of Fig. 2.7, which shows the rms value is about 10 nm again. This surface can be considered smooth since the rms values reported in $CH_3NH_3PbI_3$ values are 10 nm ~ 170 nm in the solution perovskite, and it is often stated that rms value of 10 nm as smooth in the published paper. [45-46]

In this regard, the fabricated perovskite by vacuum co-evaporation as described in the chapter 2.4, was succesed with a good morphology.

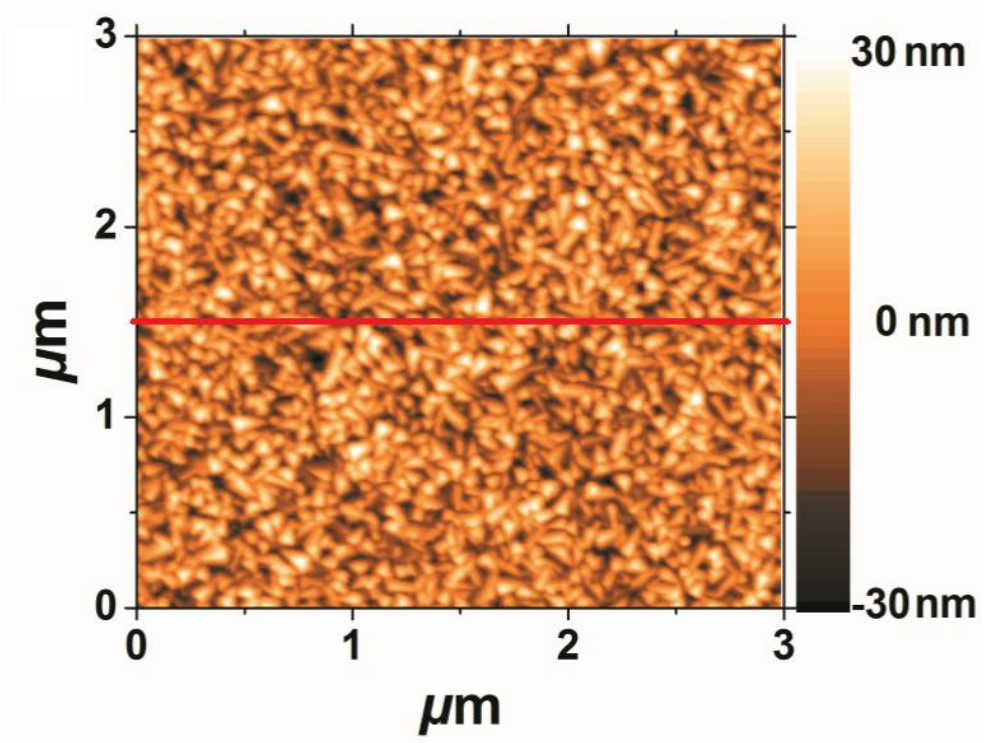

Figure 2.7. The atomic force microscope of the 320nm thick $CH_3NH_3PbI_3$ perovskite grown on the ITO/MoO_3(5 nm)/NPB(20 nm) substrate using the vacuum co-evaporation.

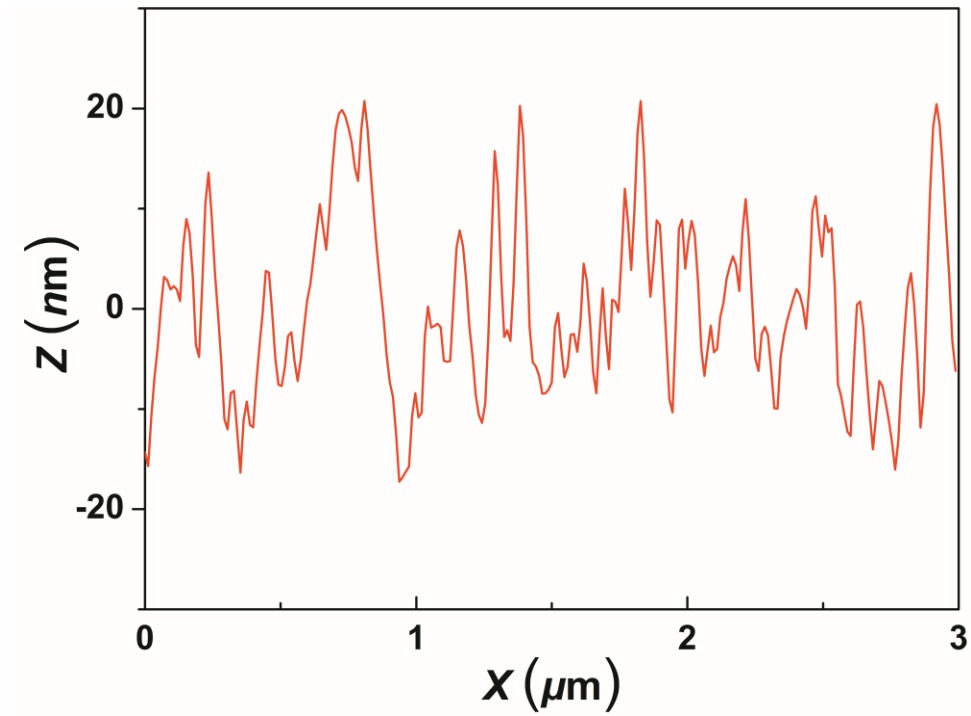

Figure 2.8. The red line profile of the AFM image in Fig. 2.7.

Chapter 3

Hole extraction layers in the vacuum processed perovskite solar cells

3.1 Introduction

The one of the most critical issues in the perovskite solar cells is HTMs since the most widely used HTM, spiro-OMeTAD possesses a few meV lower HOMO level than the VB edge of the $CH_3NH_3PbI_3$ and $CH_3NH_3PbI_{3-x}Cl_x$ [26]. This energy level mismatching causes a reduction of the $V_{OC,}$ due to the lowering in built-in field and the thermionic loss during the hole extractions as mentioned in the chapter 1.2.3. Recently there have been various reports to find the HTMs in order to achieve high performing perovskite solar cells [27-32]. However, most of the devices shows the lower performances than spioro-OMeTAD used devices except Poly(triarylamine) (PTAA) used device which shows the PCE of 16.7% [4]. The molecular structure of spiro-OMeTAD is shown in Fig. 3.1. Polander et al. recently reported fully vacuum−processed perovskite solar cells using various hole transporting layers (HTLs) and found that 2,2',7,7'-tetra(N,N -di-p -tolyl)amino-9,9-spirobifluorene (spiro-TTB) possessing HOMO level

of -5.3 eV resulted in the higher solar cell performance with V_{OC} of 1.07 V and PCE of 10.9% than spiro-OMeTAD, possessing the HOMO level of -5.0 eV which showed V_{OC} of 0.85 V and PCE of 7.7%. In this regard, one can note that the HOMO level matching HTMs can be resulted in the higher performances than spiro-OMeTAD used perovskite solar cells in the vacuum process. In this chapter, the hole extraction layer using molybdenum oxide (MoO_3) and N,N´-Bis(naphthalen-1-yl)-N,N´-bis(phenyl)benzidine (NPB) layers which are commonly used in organic light emitting diodes (OLEDs) and organic photovoltaics (OPVs) in the perovskite solar cells will be discussed.

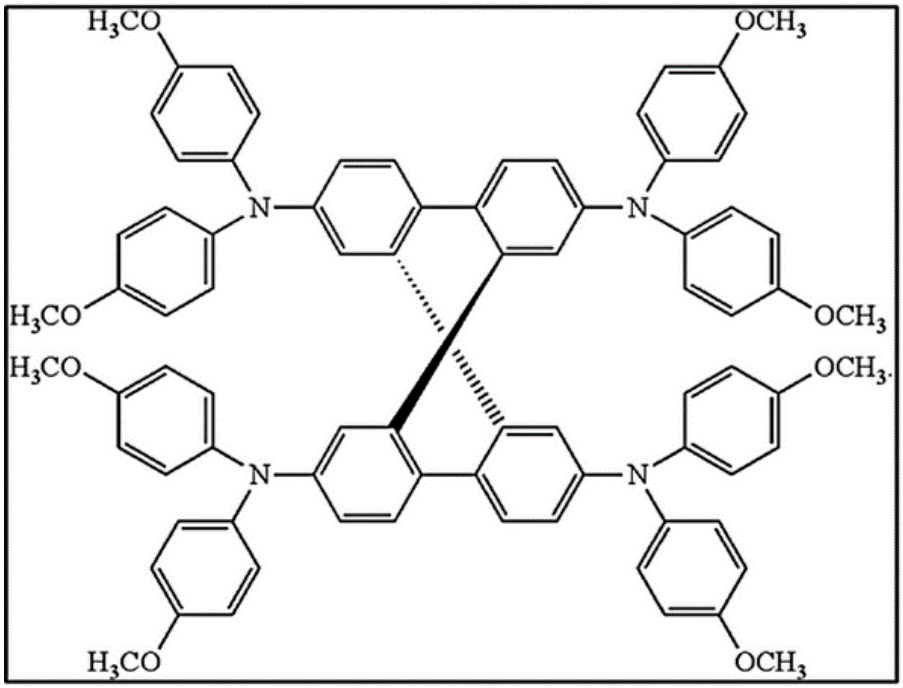

Figure 3.1. Molecular structure of spiro-2',7,7'-tetrakis-(N,N-di-p-methoxyphenylamine)-9,9'-spirobifluorene (spiro-OMeTAD).

3.2 Experiments

150 nm -thick ITO coated glass substrates were cleaned with acetone and isopropyl alcohol. All the materials except the perovskite, were thermally evaporated at the base pressure of $<1\times10^{-6}$ Torr without breaking the vacuum. The vapor pressure was increased up to 2×10^{-5} Torr when CH_3NH_3I (Jida Ruibo Optoelectronics Tech.) is deposited similar to the previous reports [23,24] as mentioned in chapter 2.2.

The deposition rate of CH_3NH_3I was monitored in real time using a crystal thickness sensor (INFICON, 5MHz) and was maintained constant during the deposition, while the deposition rate of PbI_2 (Alpha Aesar) was kept constant with 0.5 Å/s during the co-deposition. The perovskite layer was formed without any annealing process. The NPB (Nichem), C_{60} (SES Research) and BCP (Nichem) layers were deposited at a rate of 1 Å/s, and the MoO_3 (Sigma Aldrich) and the Al layers were deposited at the rates of 0.5 Å/s and 4 Å/s respectively. The deposition rates were calibrated using a profilometry (KLA-Tencor Alpha-Step IQ) before the deposition. The active area of each device was 4 mm2 and 72 devices were fabricated from 6 different batches to average the cell performance. After the evaporation, the devices were encapsulated using an epoxy resin with glass cans in an N2 environment. The UV-vis absorption spectra of the films were recorded with a VARIAN Cary 5000 UV-vis spectrophotometer. The current

density-voltage (J−V) characteristics were measured under simulated AM 1.5G sunlight of 100 mW/cm2 using Newport (91160A) solar simulator, and recorded using a Keithley 237 source measurement unit at room temperature. The light intensity was calibrated using a standard Si-solar cell (NREL). The scan step of J V characteristics was 0.02 V with 0.3 seconds of interval time for each step, and the scan direction was from negative to positive voltage. The incident photon−to−electron conversion efficiency (IPCE) was measured using a 1000 W Xe lamp combined with a monochromator and its intensity was calibrated with a Si photodiode. The IPCE was measured without light bias under the short circuit condition.

3.2 Function of the MoO_3 layer

Transition metal oxides(TMOs), such as MoO_x, ruthenium oxides (RuO_x), vanadium oxides (VO_x), tungsten oxides (WO_3) and rhenium oxide (ReO_3) with high work functions are widely used hole injection layers (HILs) in OLEDs/OPVs [47]. These high electron affinity TMOs, especially MoO_3 which shows the Fermi level of 6.01 eV in an ultra-high vacuum deposition on the indium tin oxide (ITO) substrate, causes the electron transfers from the ITO to the MoO_3 with the positive level of the vacuum level shift. Therefore the hole injection barrier, which

can be determined the difference between the Fermi level of the anode and HOMO level of the HTM can be reduced. The hole injection barrier should be considered in the perovskite solar cells similarly to the conventional OPV devices since the holes accumulated at the junction of the anode/HTM would cause the positive electric field in the forward bias. Therefore, the photo-generated holes flows against the positive field in hole extraction barrier which significantly reduces fill factor (FF). Also, forming an ohmic contact between the anode and HTM results in increase the built-in field in the fabricated photovoltaic device.

To support these functions of MoO_3 in the perovskite solar cells, the device without MoO_3 was fabricated. The device structure is ITO(150 nm)/NPB (20 nm)/perovskite (320 nm)/C_{60} (50 nm)/BCP (8 nm)/Al (100 nm). The schematic energy diagram for this structure is shown in fig. 3.2. The *J*–*V* characteristic of the fabricated device is shown in fig. 3.3. The device showed PCE of 4.2%, J_{SC} of 15.0 mA/cm^2, V_{OC} of 0.84 V and *FF* of 0.33. From the *J*–*V* characteristic, it can be seen the *s*-kink in the forward bias region which implies the injection barrier at the ITO/NPB interface as previously discussed in chapter 3.1. Also, the current density is almost zero from 1 V ~ 3 V in the forward bias region because of the injection barrier between ITO/NPB which is known as about 1.2 eV ~ 1.7 eV [47-49]. As previously mentioned in chapter 3.1, the MoO_3 forms an ohmic contact

increasing the built-in field in the devices. Therefore, without the MoO_3 layer the built-in field would be reduced and the overall solar cell performance might be degraded.

Regarding these factors above, the MoO_3 is a crucial layer in the fabricated perovskite solar cell for the hole extraction layer to enhance the solar cell performances.

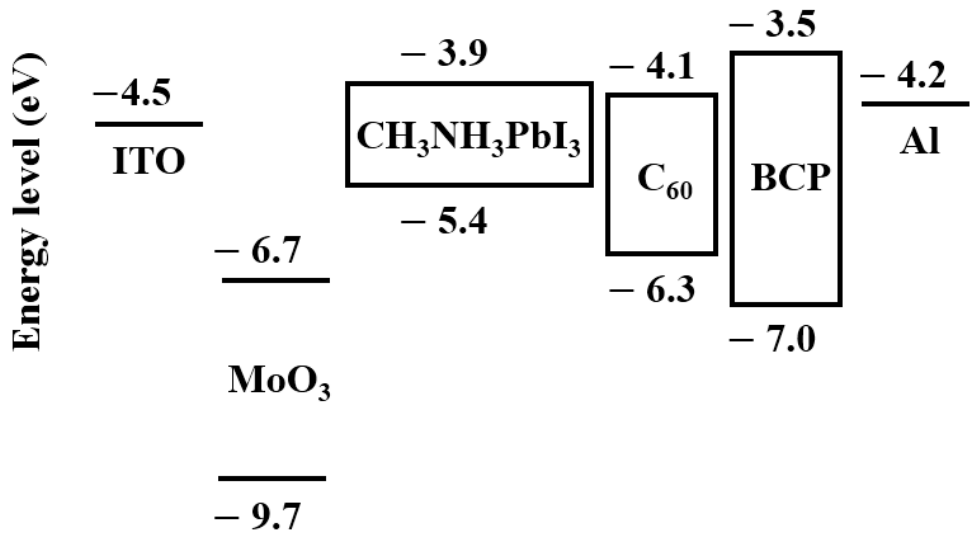

Figure 3.2. The schematic diagram of the relative energy levels of each layer in the device without MoO_3 layer. Note that the energy levels are represented against the vacuum level.

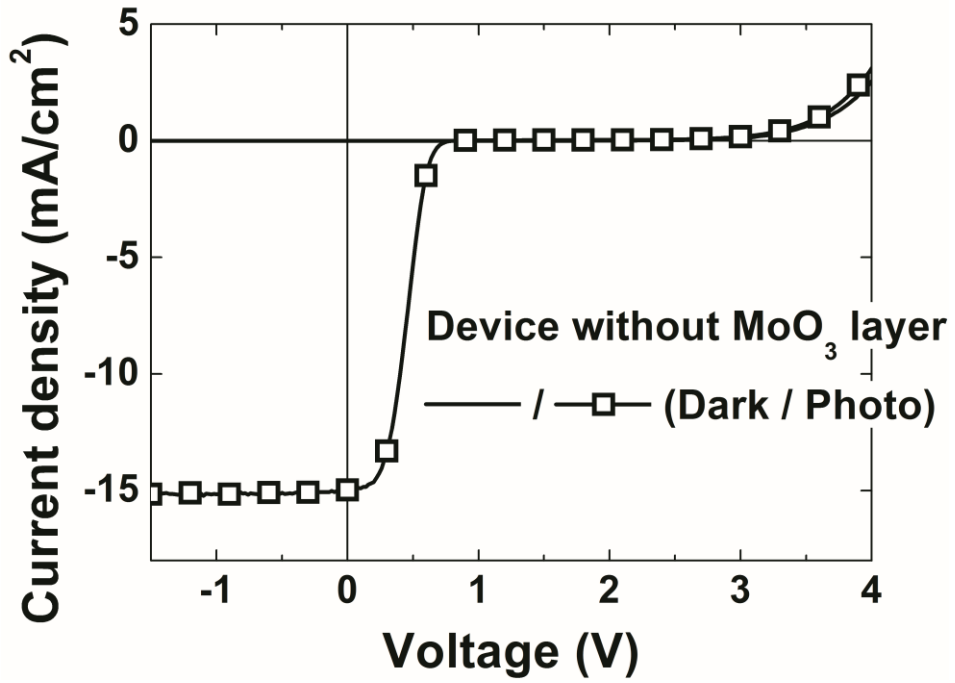

Figure 3.3. The current density−voltage *(J−V)* characteristic of the device without the MoO_3 layer. The device structure is ITO(150 nm)/NPB (20 nm)/perovskite (320 nm)/C60 (50 nm)/BCP (8 nm)/Al (100 nm).

3.3 Function of the NPB layer

In $CH_3NH_3PbI_3$, the free carriers are dominantly generated under the light bias [41]. These generated charge carriers are free to diffuse in either anode or cathode. Therefore it would be needed the charge blocking layers to collect the desired charges at the electrodes selectively [50]. In order to block the undesired charges, the energy levels should be taken into account. In the perovskite solar cell system, since the CB of $CH_3NH_3PbI_3$ is -3.9 eV, the electron blocking layer should possesses the CB or LUMO level lower than -3.9 eV. In this regard, the NPB layer which possesses the LUMO level of -2.2 eV will act as an efficient electron blocking layer enhancing the charge collection efficiency. The schematic energy diagrams of the perovskite solar cell device combined with the NPB layer is shown in fig. 3.4.

Fig. 3.5. shows the $J-V$ characteristic of the device without NPB layer. The device structure is ITO(150 nm)/MoO3(5 nm)/perovskite (320 nm)/C60 (50 nm)/BCP (8 nm)/Al (100 nm). The device showed the PCE of 6.4%, J_{SC} of 11.1 mA/cm^2, V_{OC} of 0.78 V and *FF* of 0.74. The device shoed higher FF value than the previously showed device without the MoO_3 layer shown in fig. 3.3, whereas the other parameters such as J_{SC}, and V_{OC} were reduced by 3.9 mA/cm^2 and 0.06 V comparing to the device without the MoO_3 layer.

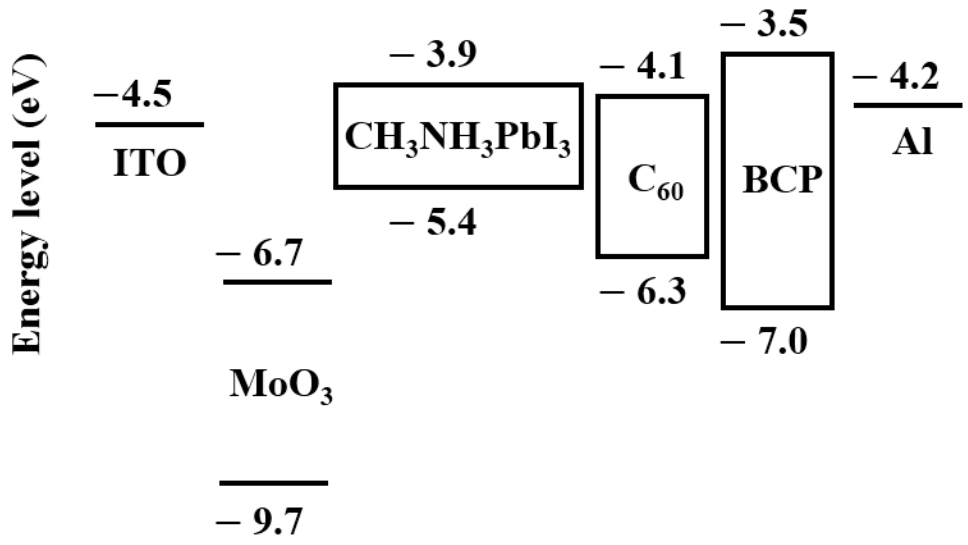

Figure 3.4. The schematic diagram of the relative energy levels of each layer in the device without NPB layer. Note that the energy levels are represented against the vacuum level.

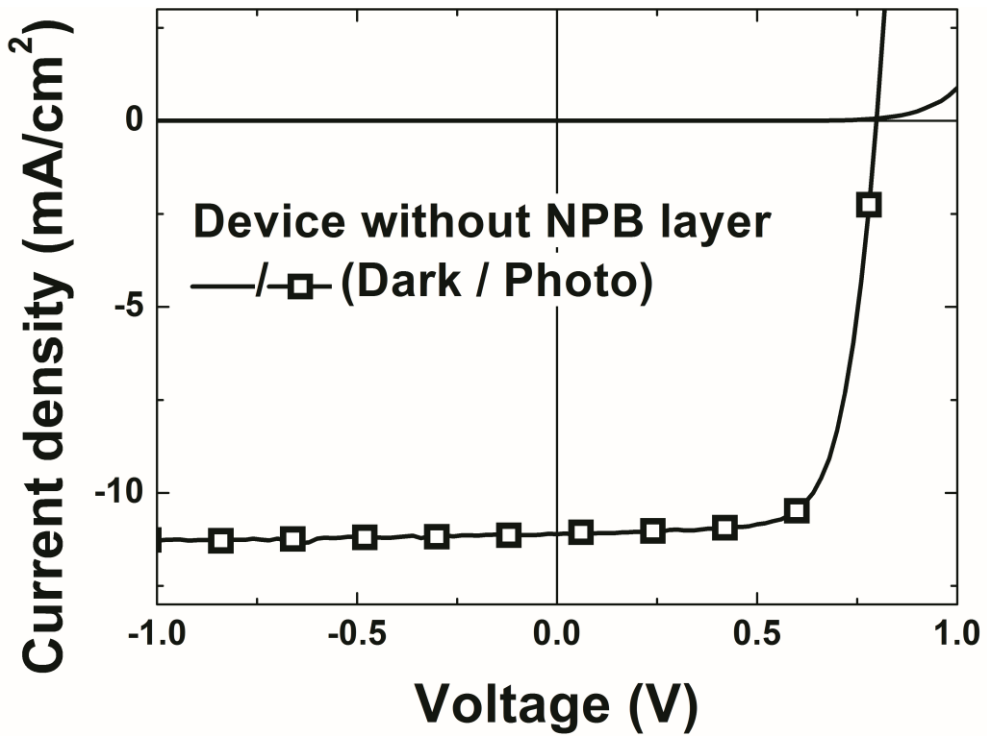

Figure 3.5. The current density−voltage *(J−V)* characteristic of the device without the NPB layer. The device structure is ITO(150 nm)/MoO_3(5 nm)/perovskite (320 nm)/C60 (50 nm)/BCP (8 nm)/Al (100 nm).

As previously mentioned in this chapter, the one of the possible reason for the lowering these parameters can be caused by the absence of the charge blocking layer. However, since the perovskite layer is known to be sensitive to the under layer there might be differences in the crystallinity or the growth modes with the different sub-layers. Fig. 3.6 shows the X-ray diffraction (XRD) patterns of the perovskite film grown on the ITO/MoO_3 (5nm) and ITO/MoO_3 (5nm)/NPB (20 nm) substrates respectively. Both films show the (110) and (220) as the main peaks at 14.06°, 28.26°. However the peak main intensities exhibit a significant difference with the different substrates. The low peak intensity on the MoO_3 sub-layer indicates that the crystallinity of the perovskite film is somehow but still oriented along [110] direction. However, the relative very strong intensity of the NPB sub-layer show that the high intensity of the main peak which implies the much higher crystallinity than on the MoO_3 sub-layer. The reason why the crystallinity is degraded on the MoO_3 layer is not clear yet. However, it can be inferred that the NPB layer can be used for a higher crystallinity in the perovskite film.

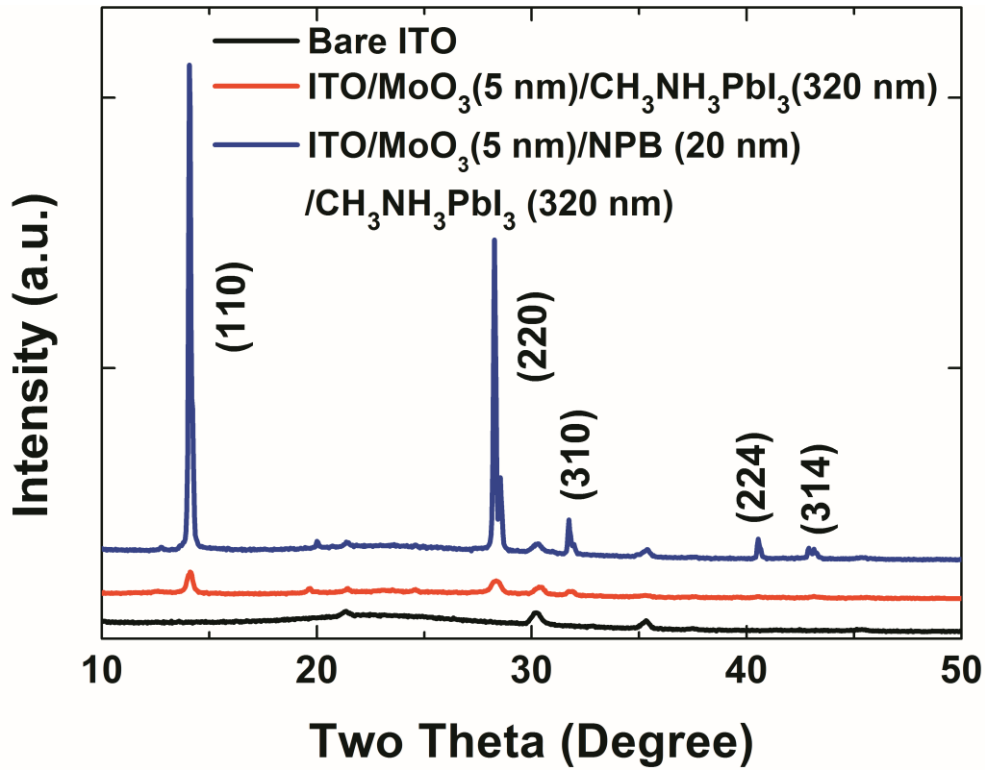

Figure 3.6. X-ray diffraction (XRD) patterns of the fabricated perovskite film on the different substrates.

Fig. 3.7 shows the AFM image of the perovskite film grown on the ITO/MoO3 (5 nm) substrate. The rms roughness was 7.2 nm and the maximum peak to valley was 62 nm from the 320 nm thick perovskite film. From these values, it is difficult to conclude the differences of the surface morphology with the different sub-layers, considering that on the NPB sub-layer the rms value was 9.7 nm and the maximum peak to valley was 70 nm as shown in fig. 2.7. However, the shape of the grain seems less sharp in MoO_3 substrate case. It is not clear yet that the sharpness of the grain is related to crystallinity of the perovskite film and also it is affected by the sub-layer.

Regarding these facts, it can be concluded that NPB layer may play 2 functions in the perovskite solar cells. The first one is that NPB layer serves as the electron blocking layer with its sufficiently lower LUMO level comparing to the CB of $CH_3NH_3PbI_3$. Also, though the reason is being investigated, the NPB layer provides a higher crystallinity than on the MoO_3 layer, which possibly originated from the preventing some chemical reactions between MoO_3 and perovskite components (e.g., Iodine, methyl ammonium) or different surface energies. To understand these correlations, more experiments and analysis will be carried out for the future works.

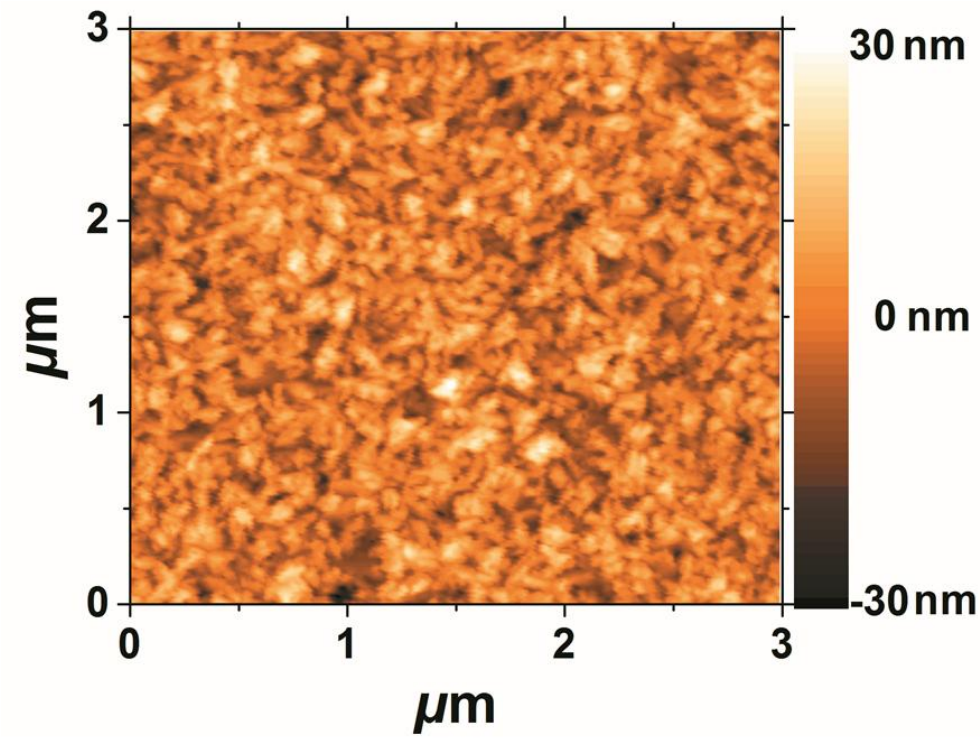

Figure 3.7. Atomic force microscope (AFM) image of the 320 nm thick perovskite film grown onto ITO/MoO_3(5 nm) substrate via vacuum co-evaporation.

3.5 Device with MoO_3/NPB layer

As previously explained in chapter 3.3 and 3.4, the MoO_3 and NPB layers are required to form an ohmic contact reducing the injection barrier, increase the built-in field, electron blocking layer and for a high crystallinities. Therefore, the device should be designed within the two layers to improve the device performances. The device structure with these two layer is ITO/MoO_3 (5 nm)/NPB (20 nm)/Perovskite (320 nm)/C_{60} (50 nm)/BCP(8 nm)/Al(100 nm). As previously mentioned, the MoO_3 and NPB layers were used as a hole extraction layer, and the perovskite was used as the light absorbing layer and charge transport layer with its high absorption coefficient and ambipolar charge transport characteristic as discussed in chapter 1.2.1. The C_{60} layer was used as the electron transporting layer and the bathocuproine (BCP) layer was used as a buffer layer which mainly acts 1) preventing Al diffusion in to C_{60} 2) preventing a dipole formation between C_{60} and Al layer and 3) formation of an ohmic contact at their interface.[51-53] . The schematic diagram of the relative energy levels of each layer in this device is shown in fig. 3.8.

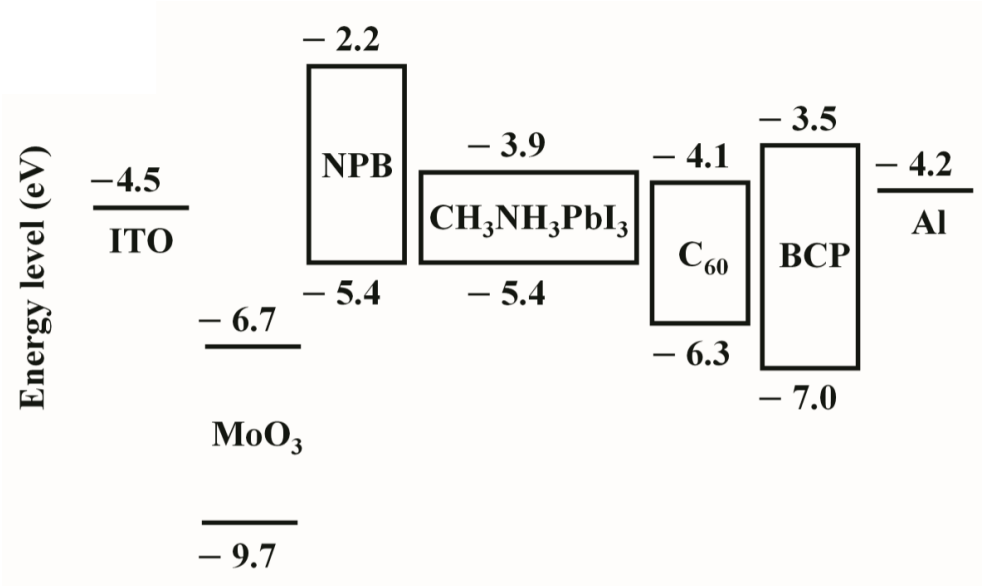

Figure 3.8. The schematic diagram of the relative energy levels of each layer in the device without MoO_3 layer. Note that the energy levels are represented against the vacuum level.

With the same structure described above, 72 devices from 6 different batches were fabricated to average the solar cell parameters. The best performing device showed the J_{SC} of 18.1 mA/cm^2, the V_{OC} of 1.12 V and the *FF* of 0.68 resulting in the PCE of 13.7% with the average values as J_{SC} of 18.5 mA/cm^2, the V_{OC} of 1.05 V and the *FF* of 0.57 resulting in the PCE of 11.1%. The $J-V$ characteristic and IPCE spectrum of the best performing device is shown in fig. 3.9 and the parameters are summarized in table 3.1.

The calculated J_{SC} by integrating the IPCE spectrum using the following equation was 17.8mA/cm2, which agrees well with the J_{SC} obtained from $J-V$ curve implying that the spectral mismatch is less than 2%.

$$J_{SC,MAX} = \int_{\lambda} \frac{hc}{q\lambda} IPCE(\lambda) I_0(\lambda) d\lambda \qquad (2)$$

I_0 : *the light intensity of the light source*

It is interesting to note that the device exhibits the high VOC of 1.12 V, which is one of the highest V_{OC} values reported up to now [2,3,5,8]. The high V_{OC} indicates that MoO_3/NPB structure works efficiently as a hole extraction layer minimizing the voltage loss. This high V_{OC} is attributed to the good alignment of the HOMO level of NPB to the VB edge of $CH_3NH_3PbI_3$. The open circuit voltage is higher than the

devices with spiro-OMeTAD (V_{OC} of 0.85 V and HOMO level of -5.0 eV) and spiro-TTB (V_{OC} of 1.07 V and HOMO level of -5.3 eV) as the HTL in the vacuum processed perovskite solar cells reported in the reference 24. One can note that the open circuit voltage increased as the HOMO level of the HTM is getting closer to the VB edge of $CH_3NH_3PbI_3$ in the vacuum processed solar cells as expected.

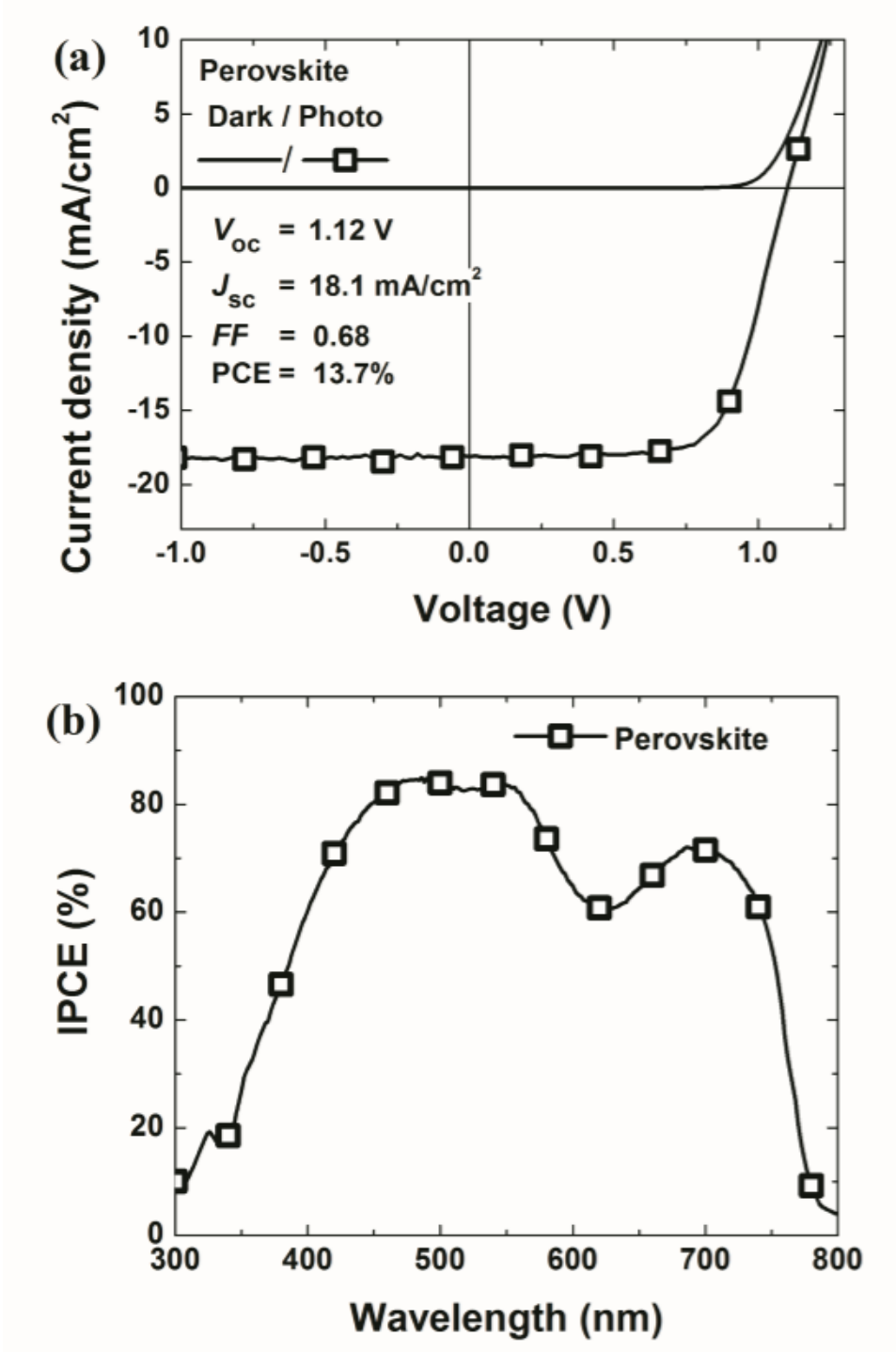

Figure 3.9. (a) The current density-voltage (*J*–*V*) characteristics and (b) incident photon-to-electron conversion efficiency (IPCE) spectrum of the best performing perovskite solar cell.

	PCE (*%*)	J_{SC} (mA/cm^2)	V_{OC} (*V*)	*FF*
Best device	13.7	18.1	1.12	0.68
Average	11.1	18.5	1.05	0.57

Table 3.1 Perovskite solar cell performance of the best performing device and the average values of the 72 devices from 6 different batches.

3.6 Conclusion

In this chapter, the perovskite solar cell comprised of ITO/MoO_3 (5 nm)/NPB (20 nm)/Perovskite (320 nm)/C_{60} (50 nm)/BCP(8 nm)/Al(100 nm) were fabricated using a full vacuum process. The best performing device showed PCE = 13.7%, J_{SC} = 18.1 mA/cm2, V_{OC} = 1.12 V, FF = 0.67 and the reproducibility is better than the normal solution processed perovskite solar cells. Importantly the considerably high V_{OC} value was obtained by employing the MoO_3/NPB layers as the hole extraction layer. This high V_{OC} is attributed to the alignment of the HOMO level of NPB to the VB edge of $CH_3NH_3PbI_3$. The fact that the MoO_3/NPB layer is widely used in OPVs/OLEDs implies that technologies developed for vacuum processed OLEDs/OPVs can be successfully applied in perovskite solar cells to accelerate the development of the perovskite solar cells. In addition since the vacuum deposition process is free from the materials restriction by their solvents, it is a promising tool to apply the various charge transport materials in the layered structures.

Chapter 4

Reproducibility of the vacuum processed perovskite solar cells

4.1 Introduction

As discussed in chapter 1.1.1, one of the critical issues of the solution processed perovskite solar cells is the reproducibility coming from the difficulties in controlling the uniformity [6-7], pin-hole formation [7-8], sensitivity to moisture and air [9-10]. Also, as mentioned in chapter 1.2.4, a variety of approaches have been introduced such as sequential deposition [2,8,11], solvent modifications [4,12-16], manipulation of the crystallization time [17,18], and changing the annealing conditions [19-22], which are mostly attempted in the modification of the solution processes to enhance the film property of the perovskite. Vacuum evaporation would be a promising method for high reproducibility and controllability due to solvent free processes combined with controllable growth parameters in a clean and inert environment [3,23-25]. Nevertheless, the fully vacuum–processed peovskite solar cells have been rarely reported up to now [25] and analysis with sufficient number of devices has never been reported. In this regard, the investigation of

the reproducibility of the fully vacuum–processed perovskite solar cell would be a meaningful work. Therefore, this chapter the reproducibility of the fully vacuum–processed perovskite solar cells will be discussed.

4.2 Histograms

Fig. 4.1 displays the histograms of (a) PCE (b) J_{SC} (c) V_{OC} and (d) FF of the 72 devices from 6 different batches. It is shown that the J_{SC} and V_{OC} are distributed within 17.2 mA/cm^2 ~ 19.5 mA/cm2 and 0.98 V ~ 1.12 V respectively, exhibiting small deviation within approximately 7% from the average values. The *FF* values show a relatively wide distribution, 0.39~0.68, hence causing the similar distribution of PCE values, 7.1%~13.7%. The origin of this variation of the FF's is not clear yet. Still the variation of the performance of the solar cells fabricated using the vacuum process is fairly narrow compared to the normal solution processed perovskite solar cells [1].

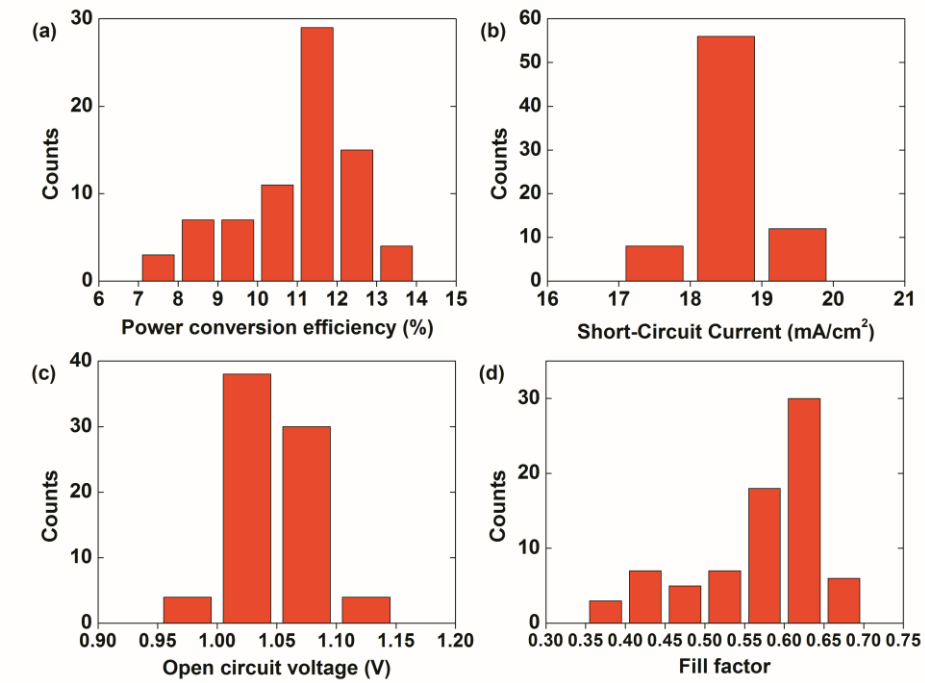

Fig. 4.1. Histogram plots of the solar cell parameters; (a) Power conversion efficiency (b) short-circuit current (c) open circuit voltage (d) fill factor of the 72 devices from 6 different batches.

4.3 Reproducibility analysis

Fig. 4.2, 4.3, 4.4, 4.5, 4.6 and 4.7 show the *J*–*V* characteristics and the average device parameters of the devices depend on the batches. The best performing, showing the highest PCE, and the worst performing, showing the lowest PCE, devices parameters and the average values in the each batch are summarized in table 4.1 to 4.6. The interesting point is that the variations of the device parameters, especially in *FF*'s, are shown in the same substrate. This means that other than the other layers, such as HTLs, ETL, buffer layer and the cathode metal, the perovskite layer would be the crucial reason for the variation of the *FF* values. The possible origin of this variation is the behavior of the MAI, as discussed in chapter 2.1, showing a gas-like behavior in the vacuum chamber when it is deposited. If the experiment carried out with deposition of MAI in a more controllable way, the FF values would show a narrow distribution with the high reproducibility in overall solar cell parameters in vacuum processed perovskite solar cells.

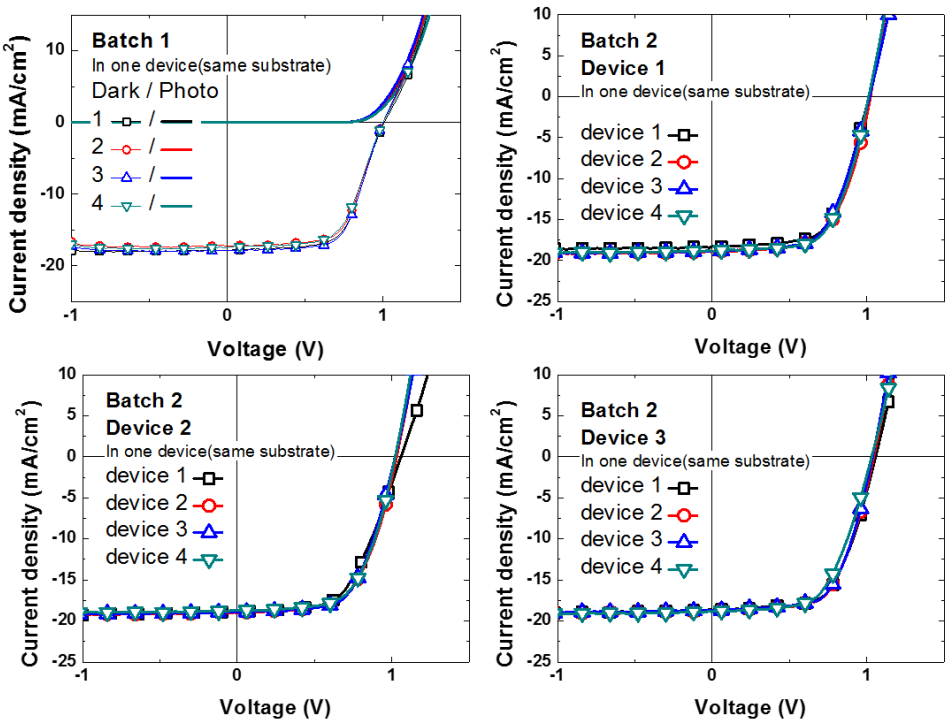

Fig. 4.2. Current density−Voltage (J−V) characteristics of the fabricated perovskite solar cells in batch 1 and 2.

Table 4.1 Device parameters of the best, worst performing devices and the average values of batch 1.

	PCE (%)	J_{SC} (mA/cm^2)	V_{OC} (V)	*FF*
Best	11.44	17.8	1.02	0.63
Worst	10.7	17.4	1.02	0.60
Average	11.1	17.5	1.01	0.63

Table 4.2 Device parameters of the best, worst performing devices and the average values of batch 2.

	PCE (%)	J_{SC} (mA/cm^2)	V_{OC} (V)	*FF*
Best	12.3	18.9	1.06	0.62
Worst	11.0	17.9	1.06	0.58
Average	11.8	18.7	1.03	0.61

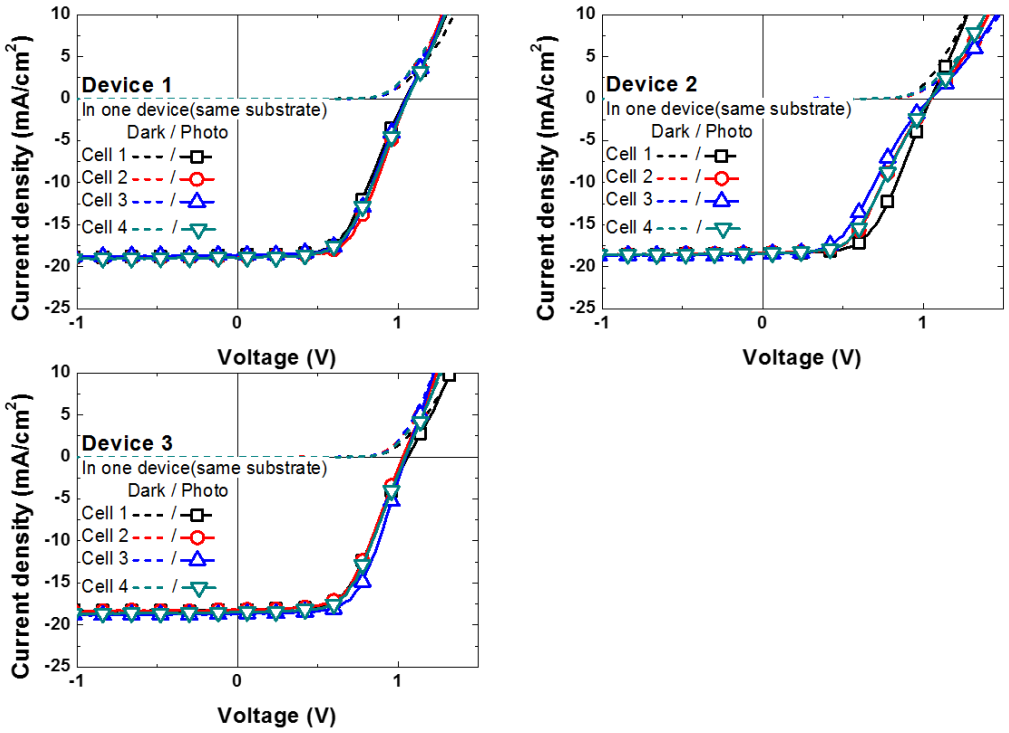

Fig. 4.3. Current density−Voltage (J−V) characteristics of the fabricated perovskite solar cells in batch 3.

Table 4.3 Device parameters of the best, worst performing devices and the average values of batch 2.

	PCE (%)	J_{SC} (mA/cm^2)	V_{OC} (V)	*FF*
Best	12.0	18.7	1.05	0.61
Worst	9.4	18.4	1.05	0.49
Average	10.6	18.5	0.05	0.54

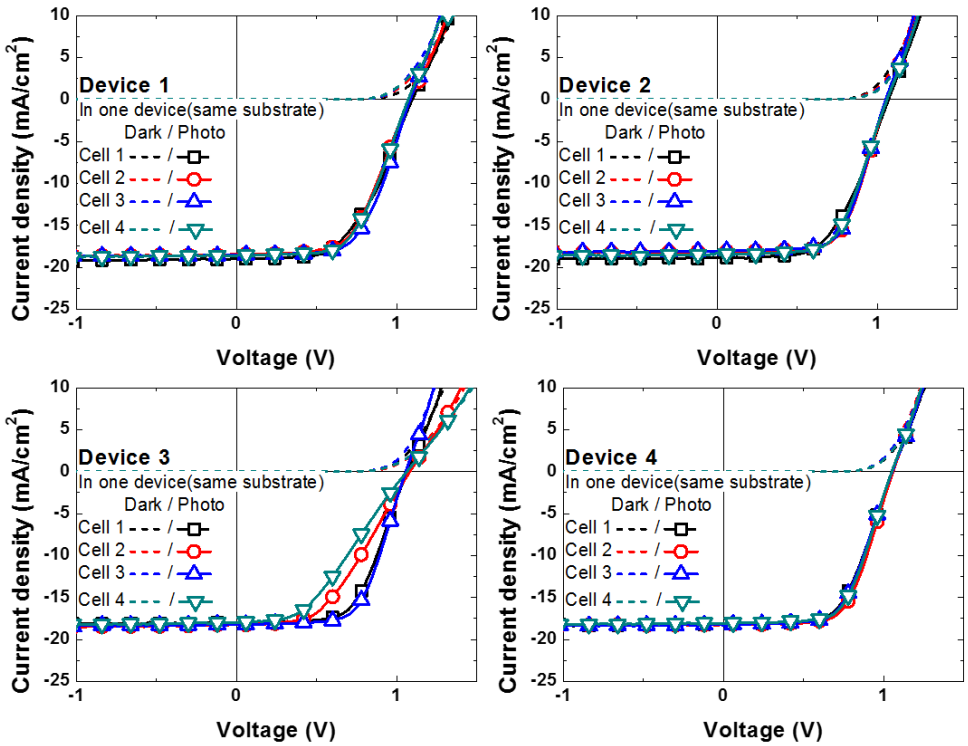

Fig. 4.4. Current density−Voltage (J−V) characteristics of the fabricated perovskite solar cells in batch 4.

Table 4.4 Device parameters of the best, worst performing devices and the average values of batch 2.

	PCE (%)	J_{SC} (mA/cm^2)	V_{OC} (V)	*FF*
Best	12.2	18.3	1.04	0.64
Worst	7.6	18.0	1.08	0.39
Average	11.4	18.3	1.07	0.58

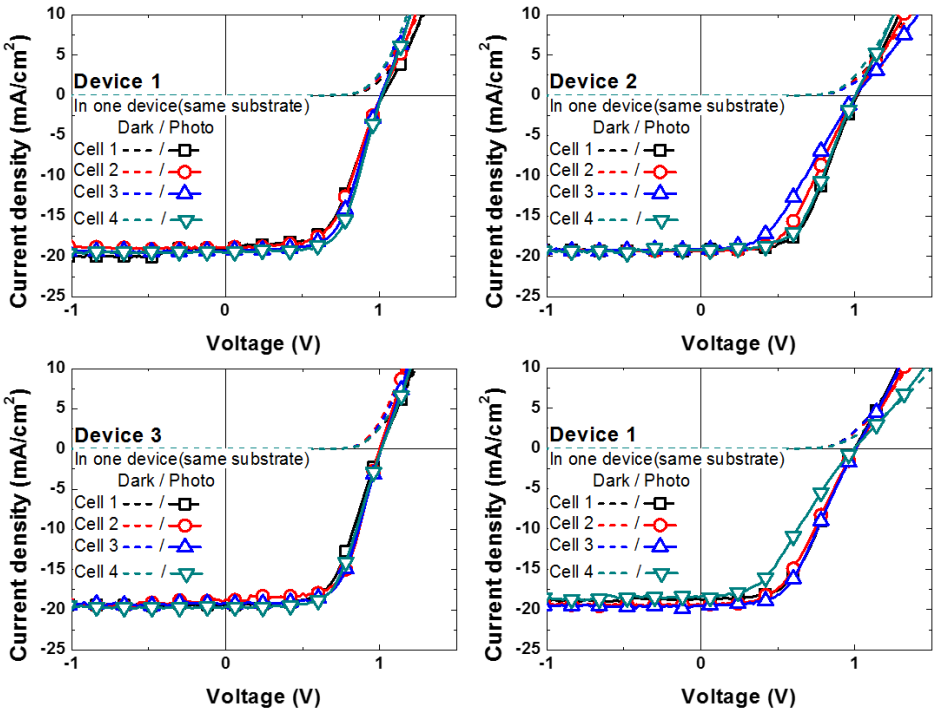

Fig. 4.5. Current density−Voltage (J−V) characteristics of the fabricated perovskite solar cells in batch 5.

Table 4.5 Device parameters of the best, worst performing devices and the average values of batch 2.

	PCE (%)	J_{SC} (mA/cm^2)	V_{OC} (V)	*FF*
Best	12.6	19.6	1.00	0.64
Worst	7.1	18.4	0.98	0.39
Average	10.5	19.2	1.01	0.54

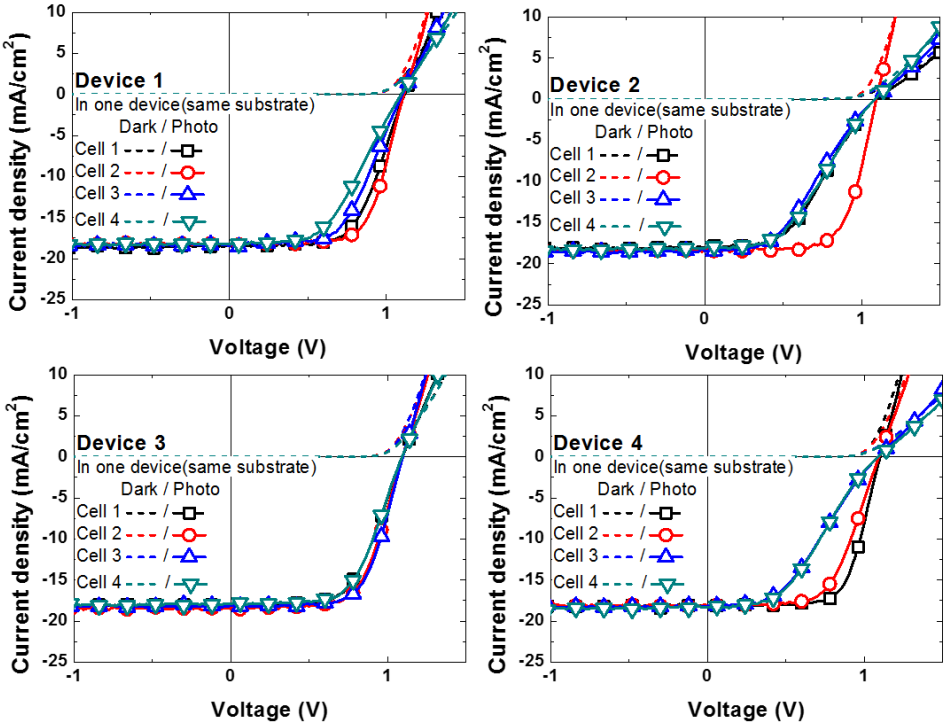

Fig. 4.6. Current density−Voltage (J−V) characteristics of the fabricated perovskite solar cells in batch 6.

Table 4.6 Device parameters of the best, worst performing devices and the average values of batch 2.

	PCE (%)	J_{SC} (mA/cm^2)	V_{OC} (V)	*FF*
Best	13.7	18.1	1.12	0.67
Worst	8.1	18.5	1.10	0.40
Average	11.1	18.2	1.10	0.56

4.4 Conclusion

As shown in the previous chapter, the vacuum processed perovskite cells demonstrated the distribution of 17.2 mA/cm^2~19.5 mA/cm^2 in J_{SC}, and 0.98 V~1.12 V of V_{OC} respectively, exhibiting small deviation within approximately 7% from the average values. The *FF* values show a relatively wide distribution, 0.39~0.68, hence causing the similar distribution of PCE values, 7.1%~13.7%. This reproducibility is comparably higher than the normal solution processed perovskite. However, recently a few reports demonstrated high reproducibility via modification of the solution processes such as deposition of PbI_2 two times [12] and slowing down the MAI-PbI_2 reaction [4, 17]. Considering that the film properties of the perovskite and the reproducibility have been improved by the modification in the deposition process and we used the plain vacuum process without any further treatments, if the modifications done in the solution process is carried, the vacuum process will result in the better reproducibility.

Chapter 5

Hysteresis behavior of the vacuum processed perovskite solar cells

5.1 Introduction

The hysteresis behaviour is well known issue in the perovskite based solar cell fields [4,54-56]. The hysteresis in perovskite solar cells is anomalous because in other photovoltaic devices such as silicon based solar cells, the hysteresis is observed in the extremely fast scan rates performed in less than 2 to 44 ms, correspond to the scan rate of 15 to 300 V/s [54, 55], whereas the hysteresis in the perovskite solar cells is observed in the very slow scan rates less than 0.3 V/s and even becomes stronger as the rate decreases [54]. In addition, since the difference scan direction yields the different solar cell parameters the hysteresis effect should be taken into account to report the accurate solar cell performances. Therefore, in this chapter the hysteresis effects of the fabricated perovskite solar cells would be discussed.

5.2 *J–V* characteristics with different scan directions

Fig. 5.1 shows the *J–V* characteristics with the different scan directions. The scan step was 0.02 V and the step of the each voltage was 300 ms. As shown in fig. 5.1, the vacuum processed perovskite solar cell showed the hysteresis. The main difference caused from the *FF*, which showed 0.62 in forward scan, short circuit to open circuit direction, and 0.56 in the reverse scan, open circuit voltage to short circuit direction. On the other hand, the J_{SC} values were 18.1 mA/cm^2 and 17.1 mA/cm^2, V_{OC} values were 1.09 V and 1.07 V for the forward and reverse scans respectively, which showed the less difference than *FF*. These different scan directions result in the differences of 6% in J_{SC}, 1.9% in V_{OC}, 11% in FF and 17% in PCE.

It has been reported that in the mesoscopic structure the hysteresis is observed as well as in the planar heterojunction structure the hysteresis might be observed. The *FF* degradation in the reverse scan implies that the generated charge carriers are not extracted to the external circuit and the reasons are not clear yet. The plausible origins would be discussed in the next chapter.

,

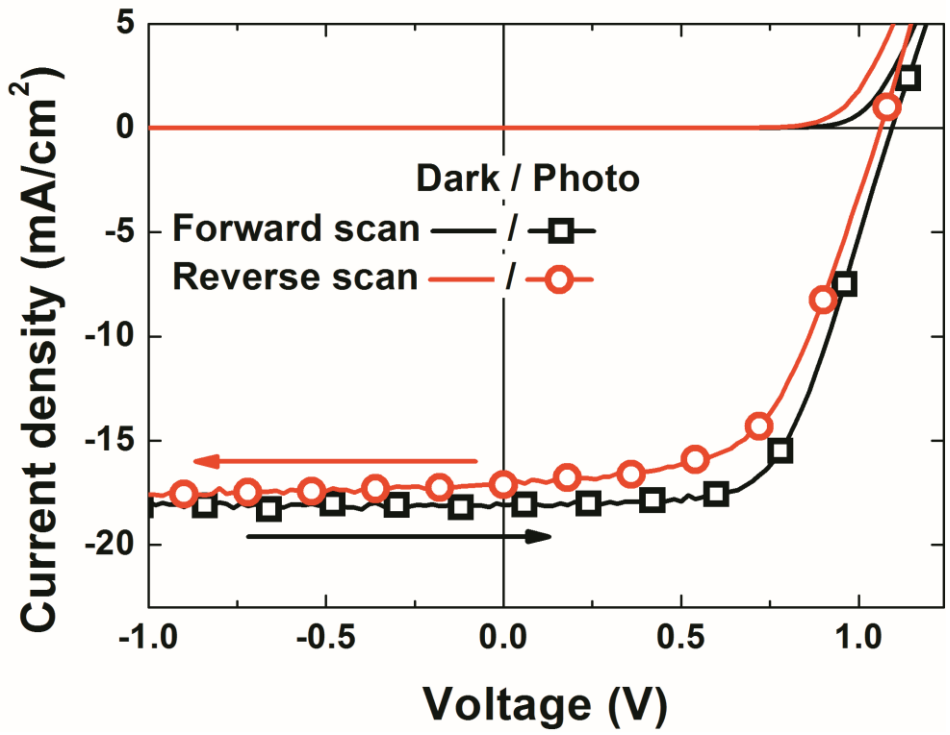

Fig. 5.1. The current density-voltage ($J-V$) characteristics of a device with the MoO_3/NPB layer for different scan directions. The device structure is ITO (150 nm)/MoO_3 (5 nm)/NPB (20 nm) $CH_3NH_3PbI_3$ (320 nm)/C_{60} (50 nm)/BCP (8 nm)/Al (100 nm).

Table 5.1 The solar cell parameters of the device with the MoO_3/NPB layer shown in fig. 5.1 with different scan directions.

Scan directions	*PCE* (%)	J_{SC} (mA/cm^2)	V_{OC} (V)	*FF*
Forward	12.1	18.1	1.09	0.62
Reverse	10.3	17.1	1.07	0.56

To investigate the effect of the HTLs on the hysteresis behavior, the devices without MoO_3 or NPB layers were measured in different scan directions of the J–V characteristic. As shown in fig. 5.2 the device without MoO3 layer shows the hysteresis as well as in the case of the device shown in fig. 5.1, with the MoO_3/NPB layer. The solar cell parameters were differed with difference scan directions, J_{SC} of 2.3% of V_{OC}, 10% of *FF* and 12.5% of PCE. In addition, the device without NPB layer showed the hysteresis as well shown in fig. 5.3. In the similar way to the device without MoO_3 layer, the differences of the J_{SC}, V_{OC}, FF and PCE were 4.5%, 12%, 1.3% and 7.8% respectively. It is interesting to note that unlike to the previous cases, the *FF* showed the least variation in different scan directions. In addition, the *FF* value in the case of the without NPB, is the highest among the devices with MoO_3/NPB or NPB layer in the fabricated solar cell. The value 0.74 and 75 in the fig. 5.3, is even higher than the best performing device with PCE of 13.7% which shows the *FF* of 0.68. Regarding these facts, the higher fill factor gives smaller hysteresis, and the parameter affecting the fill factor would be the one of the crucial reasons for the hysteresis.

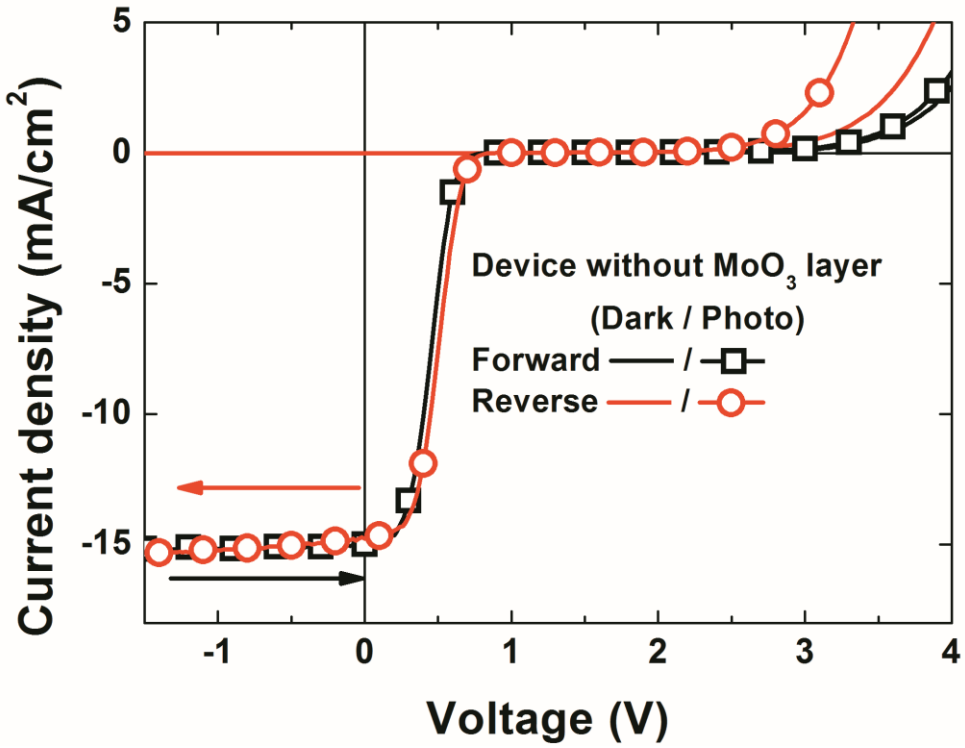

Fig. 5.2. The current density-voltage ($J-V$) characteristics of a device without the MoO_3 layer for the different scan directions. The device structure is ITO (150 nm)/NPB (20 nm) $CH_3NH_3PbI_3$ (320 nm)/C_{60} (50 nm)/BCP (8 nm)/Al (100 nm).

Table 5.2 The solar cell parameters of the device without the MoO_3 layer shown in fig. 5.2 with different scan directions.

Scan directions	*PCE* (%)	J_{SC} (mA/cm^2)	V_{OC} (V)	*FF*
Forward	4.2	15.0	0.84	0.33
Reverse	4.8	14.8	0.86	0.37

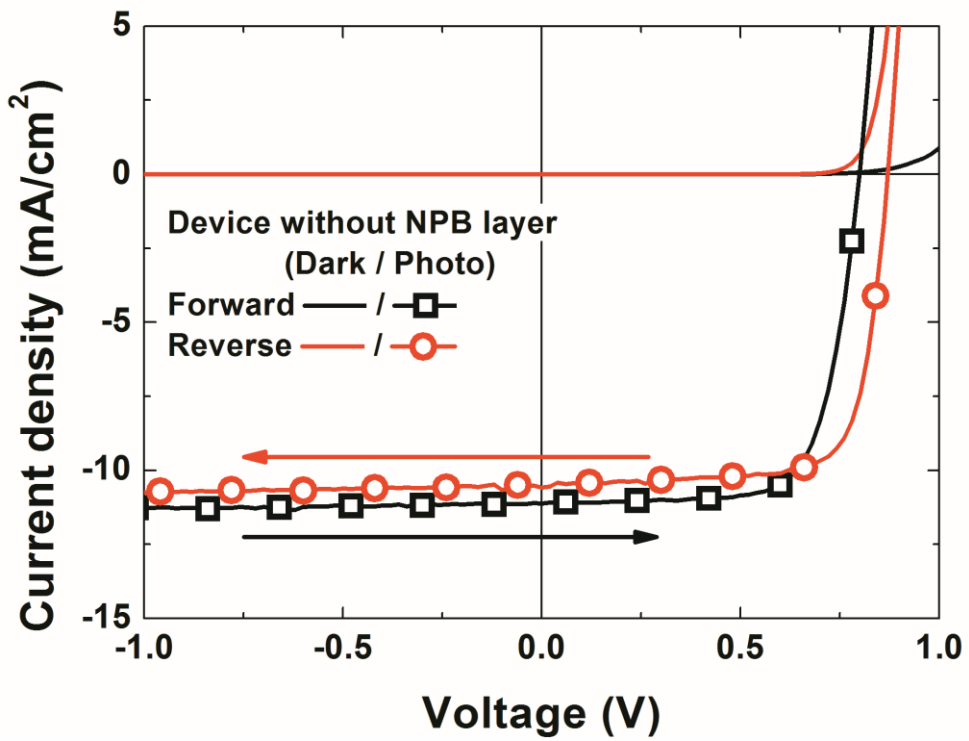

Fig. 5.3. The current density-voltage ($J-V$) characteristics of a device without the NPB layer for the different scan directions. The device structure is ITO (150 nm)/MoO_3(5 nm)/$CH_3NH_3PbI_3$ (320 nm)/C_{60} (50 nm)/BCP (8 nm)/Al (100 nm).

Table 5.3 The solar cell parameters of the device without the NPB layer shown in fig. 5.3 with different scan directions.

Scan directions	*PCE* (%)	J_{SC} (mA/cm^2)	V_{OC} (V)	*FF*
Forward	6.4	11.1	0.78	0.74
Reverse	6.9	10.6	0.87	0.75

5.3 Plausible origins

As discussed, the hysteresis behaviour is usually observed in the perovskite solar cells as well as our device. The clear reason has not been figured out exactly but there are some theories to explain the hysteresis behaviour as follows. [4, 54]

1) Interface traps
2) Ferroelectricity of the perovskite
3) Excessive mobile ions
4) Space charge in the charge transport layers

The first hypothesis is based on the experiment that the hysteresis behaviour enhances without the charge transport layers [54]. Therefore, there could be some interfacial traps and the trap filling and de-trapping time from short circuit to open circuit and open circuit to short circuit will be different which cause the hysteresis behaviour. However, a few papers with plnanrheterojunction perovskite solar cells reports that the hysteresis was not observed [8, 25]. Therefore, if the hysteresis is originated from the own bulk property of the perovskite, the hysteresis should be observed regardless the device structure which is not in experimentally. The third reason would be taken into account if the composition of the perovskite is different laboratory to laboratory and these excessive/deficient components generates the mobile ions, the

hysteresis can be observed. The fourth reason was argued based on the experiment results that the hysteresis is varied with the different thickness of the mesoporous TiO_2 layer. However, if the thicker charge transport layer causes the space charge and this is attributed to the hysteresis, the hysteresis should be reduced without the MoO_3 or NPB layer which cannot be applied to the our result, as well as the result that the hysteresis was increased without the charge transport layers [54].

5.3 Conclusion

In conclusion, the origin of the variations in different scan direction is not clear, but among the suggested hypothesis the interfacial trap is the most suspicious factor for the observed hysteresis in our device since other theories such as the ferroelectricity, excessive mobile ions and the space charge in the charge transport layers contradict to other reports and our results. The systematic investigation of the origin should be investigated for the future work.

Chapter 5

Summary and outlooks

In this thesis, the fully vacuum－processed perovskite solar cells were demonstrated with the detail procedure of the method to fabricate the high quality films, analyzing the hole extraction layers in the perovskite solar cells and the device characterizations, reproducibility and the hysteresis.

In chapter 1, the brief introduction of the perovskite solar cell fields and the material properties of the commonly used organometal halide perovskites were described. In addition, the basic principle of the perovskite device and fabrication methods of the perovskite films were discussed.

In chapter 2, the detail methodology to fabricate the high quality perovskite films using the vacuum co-evaporation was explained. It was shown that the process and methodology to obtain the chemically balanced perovskite there is a difference between the mixed halide perovskite ($CH_3NH_3PbI_{3-x}Cl_x$) and triiodie perovskite ($CH_3NH_3PbI_3$). Moreover, the deposition condition significantly affects the properties of the film, especially the morphology.

In chapter 3, the effects of the MoO_3 and NPB layers on the perovskite based device were investigated. The MoO_3 layer is required to form an ohmic contact between the anode (ITO) and the HTM (NPB) and reducing the hole injection barrier. This has been supported from the *J*–*V* characteristic of the device without MoO_3 layer which showed the *s*–kink result in the PCE of 4.2%, J_{SC} of 15.0 mA/cm^2, V_{OC} of 0.84 and *FF* of 0.33. The device without NPB layer was also investigated and the device showed the PCE of 6.4%, J_{SC} of 11.1 mA/cm^2, V_{OC} of 0.78 and *FF* of 0.74. Interestingly, the *FF* was significantly increased comparing to the device without MoO_3 layer. The roles of the NPB layer are thought to be as the electron blocking layer since NPB possesses the LUMO level of -2.2 eV which is sufficiently lower than the CB of the perovskite (-3.9 eV). The other possible effects of the NPB layer, such as the crystallinity and the morphology was investigated. The crystallinity showed decrease on the MoO_3 substrate comparing to the NPB substrate with negligible differences in the rms roughness and peak to valley values. The combination of the MoO_3 and NPB layers significantly improves the device performances showing the PCE of 13.7%, J_{SC} of 18.1 mA/cm^2, V_{OC} of 1.12 and *FF* of 0.68. Importantly the considerably high V_{OC} value was obtained by employing the MoO_3/NPB layers as the hole extraction layer. This high V_{OC} is attributed to the alignment of the HOMO level of NPB to the VB edge of $CH_3NH_3PbI_3$.

In chapter 4, the reproducibility of the vacuum processed perovskite solar cells was discussed. It was shown that the J_{SC} and V_{OC} are distributed within 17.2 mA/cm^2 ~ 19.5 mA/cm^2 and 0.98 V ~ 1.12 V respectively, exhibiting small deviation within approximately 7% from the average values. The *FF* values show a relatively wide distribution, 0.39~0.68, hence causing the similar distribution of PCE values, 7.1%~13.7%. Still the variation of the performance of the solar cells fabricated using the vacuum process is fairly narrow compared to the normal solution processed perovskite solar cells. Finding the origin of the variation of *FF* will be carried out to enhance the better reproducibility.

In chapter 5, the hysteresis behavior of the fabricated perovskite solar cells and the plausible origins were discussed. The devices with the NPB/MoO_3 layer, without the NPB layer and without the MoO_3 layer showed the hysteresis regardless the device architecture. However, the device with MoO_3/NPB layer showed degraded performance in the reverse scan, sweeping from the open circuit to the short circuit condition, whereas there was a slight increase of the PCE in the devices without MoO_3 or NPB layers. The one of the suspicious origin is the interfacial trap sites, however it is not clear yet to explain the observed hysteresis behavior in our results. This should be investigated for the future work to find out the origin of the hysteresis, which result in a deeper understanding the fundamental physics of the perovskite solar

cells.

In this thesis, the application of MoO_3/NPB, which is typically used in the vacuum processed OLEDs/OPVs, into the perovskite solar cells using the full vacuum process has been demonstrated successfully. The fact that the MoO_3/NPB layer is widely used in OPVs/OLEDs implies that technologies developed for vacuum processed OLEDs/OPVs can be successfully applied in perovskite solar cells to accelerate the development of the perovskite solar cells. In addition since the vacuum deposition process is free from the materials restriction by their solvents, we believe that our works suggest the promising tool to apply the various charge transport materials in the layered structures, extending the research area of the perovskite solar cell.

Bibliography

1. M. M. Lee, J. Teuscher, T. Miyasaka, T. N. Murakami, H. J. Snaith, Science 338 (2012) 643.
2. J. Burschka, N. Pellet, S.-J. Moon, R. Humphry-Bake, P. Gao, M. K. Nazeeruddin, M. Grätzel, Nature 499 (2013) 316.
3. M. Liu, M. B. Johnston, H. J. Snaith, Nature 501 (2013) 395.
4. N. J. Jeon, J. H. Noh, Y. C. Kim,W. S. Yang, S. Ryu, S. I. Seok, Nature Mater. 13 (2014) 897–903.
5. H. Zhou, Q. Chen, G. Li, S. Luo, T.-B Song, H.-S. D, Z. Hong, J. You, Y. Liu, Y. Yang, Science 345 (2014) 542.
6. D. Bi, S.-J. Moon, L. Häggman, G. Boschloo, L. Yang, E. M. J. Johansson, M. K. Nazeeruddin, M. Grätzel, A. Hagfeldt, RSC Adv. 3 (2013) 18762–18766.
7. J. M. Ball, M. M. Lee, A. Hey, H. J. Snaith, Energy Environ. Sci. 6 (2013) 1739-1743.
8. Z. Xiao, C. Bi, Y. Shao, Q. Dong, Q. Wang, Y. Yuan, C. Wang, Y. Gao, J. Huang, Energy Environ. Sci. 7 (2014) 2619.
9. J. H. Noh, S. H. Im, J. H. Heo, T. N. Mandal, S. I. Seok, Nano Lett. 13 (2013) 1764–1769.
10. G. Niu, W. Li, F. Meng, L. Wang, H. Dong, Y. Qiu, J. Mater. Chem. A. 2 (2014) 705.
11. Q. Chen, H. Zhou, Z. Hong, S. Luo, H.-S Duan, H.-H. Wang, Y.

Liu, G. Li, Y. Yang, J. Am. Chem. Soc. 136 (2014) 622–625.

12. J. Shi, Y. Luo, H. Wei, J. Luo, J. Dong, S. Lv, J. Xiao, Y. Xu, L. Zhu, X. Xu, H. Wu, D. Li, Q. Meng, ACS Appl. Mater. Interfaces 6 (2014) 9711–9718.

13. B. Conings, L. Baeten, C. D. Dobbelaere, J. D'Haen, J. Manca, H.-G. Boyen, Adv. Mater. 26 (2014) 2041–2046.

14. J.-H. Im, C.-R. Lee, J.-W Lee, S.-W. Park, N.-G. Park, Nanoscale 3 (2011) 4088.

15. H.-B. Kim, H. Choi, J. Jeong, S. Kim, B. Walker, S. Song, J. Y. Kim, Nanoscale 6 (2014) 6679-6683.

16. Y. Zhao, K. Zhu, J. Phys. Chem. C 118 (2014) 9412–9418.

17. Y. Wu, A. Islam, X. Yang, C. Qin, J. Liu, K. Zhang, W. Penga, L. Han, Energy Environ. Sci. 7 (2014) 2934-2938.

18. M. Xiao, F. Huang, W. Huang, Y. Dkhissi, Y. Zhu, J. Etheridge, A. Gray-Weale, U. Bach, Y. B. Cheng, L. Spiccia, Angew. Chem. Int. Ed. 126 (2014) 10056–10061.

19. G. E. Eperon, V. M. Burlakov, P. Docampo, A. Goriely, H. J. Snaith, Adv. Funct. Mater. 24 (2014) 151–157.

20. A. Dualeh, N. Tétreault, T. Moehl, P. Gao, M. K. Nazeeruddin, M. Grätzel, Adv. Funct. Mater. 24 (2014) 3250–3258.

21. M. Saliba, K. W. Tan, H. Sai, D. T. Moore, T. Scott, W. Zhang, L. A. Estroff, U. Wiesner, H. J. Snaith, J. Phys. Chem. C 118 (2014) 17171–17177.

22. Z. Xiao, Q. Dong, C. Bi, Y. Shao, Y. Yuan, J. Huang, Adv. Mater. (2014) DOI: 10.1002/adma.201401685.

23. O. Malinkiewicz, A. Yella, Y. H. Lee, G. M. Espallargas, M. Grätzel, M. K. Nazeeruddin, H. J. Bolink, Nat. Photonics 8 (2014) 128.

24. L. E. Polander, P. Pahner, M.Schwarze, M. Saalfrank, C. Koerner, K. Leo, APL Mater. 2 (2014) 081503.

25. C.-W. Chen, H.-W. Kang, S.-Y. Hsiao, P.-F. Yang, K.-M. Chiang, H.-W. Lin, Adv. Mater. 26 (2014) 6647–6652.

26. P. Schulz, E. Edri, S. Kirmayer, G. Hodes, D. Cahen, A. Kahn, Energy Environ. Sci. 7 (2014) 1377–1381.

27. N. J. Jeon, H. G. Lee, Y. C. Kim, J. Seo, J. H. Noh, J. Lee, S. I. Seok, J. Am. Chem. Soc. 136 (2014) 7837–7840.

28. P. Qin, N. Tetreault, M. I. Dar, P. Gao, K. L. McCall, S. R. Rutter, S. D. Ogier, N. D. Forrest, J. S. Bissett, M. J. Simms, A. J. Page, R. Fisher, M. Grätzel, M. K. Nazeeruddin, Adv. Energy Mater. (2014) DOI: 10.1002/aenm.201400980.

29. K.-G. Lim, H.-B. Kim, J. Jeong, H. Kim, J. Y. Kim, T.-W. Lee, Adv. Mater. (2014) DOI: 10.1002/adma.201401775.

30. Y. S. Kwon, J. Lim, H.-J. Yun, Y.-H. Kim, T. Park, Energy Environ. Sci. 7 (2014) 1454-1460.

31. J.-Y. Jeng, K.-C. Chen, T.-Y. Chiang, P.-Y. Lin, T.-D. Tsai1, Y.-C. Chang, T.-F. Guo, P. Chen, T.-C. Wen, Y.-J. Hsu, Adv. Mater. 26

(2014) 4107-4113

32. A. Krishna, D. Sabba, H. Li, J.Yin, P. P. Boix, C. Soci, S. G. Mhaisalkar, A. C. Grimsdale, Chem. Sci. 5 (2014) 2702-2709.

33. G. E. Eperon, S. D. Stranks, C. Menelaou, M. B. Johnston, L. M. Herz, H. J. Snaith, Energy Environ. Sci. (2014) 7, 982.

34. J.-W. Lee, D.-J. Seol, A.-N. Cho, N.-G. Park, Adv. Mater. (2014) 26, 4991.

35. N. K. Noel, S. D. Stranks, A. Abate, C. Wehrenfennig, S. Guarnera, A. A. Haghighirad, A. Sadhanala, G. E. Eperon, M. B. Johnston, A. M. Petrozza, L. M. Herz, H. J. Snaith, Energy Environ. Sci. (2014) 7, 3061-3068.

36. F. Hao, C. C. Stoumpos, D. H. Cao, R. P. H. Chang, M. G. Kanatzidis, Energy Environ. Sci. (2014) 7, 3061-3068.

37. W.-J. Yin, T. Shi, Y. Yan, Adv. Mater., (2014), 26, 4653–4658.

38. G. Xing, N. Mathews, S. Sun, S. S. Lim,Y. M. Lam, M. Grätzel, S. Mhaisalkar, T. C. Sum, Science (2013) 342, 344

39. S. D. Stranks, G. E. Eperon, G. Grancini, C. Menelaou, M. J. P. Alcocer, T. Leijtens, L. M. Herz, A. Petrozza, H. J. Snaith, Sience (2013) 342 341

40. T. Ishihar, J. Lumin. (1994), 60−1, 269−274.

41. V. D'Innocenzo, G. Grancini, M. J. P. Alcocer, A. R. S. Kandada, S. D. Stranks, M. M. Lee, G. Lanzani, H. J. Snaith, A. Petrozza, Nature Comm. (2014) 5, 3586.

42. A. Marchioro, J. Teuscher, D. Friedrich, M. Kunst, R. v. d. Krol, Nature Photonics (2014), 8, 250–255

43. .D. Bi, L. Yang, G. Boschloo, A. Hagfeldt, E. M. J. Johansson, J. Phys. Chem. Lett. (2013) 4, 1532−1536

44. S. Colella, E. Mosconi, P. Fedeli, A. Listorti, F. Gazza, F. Orlandi, P. Ferro, T. Besagni, A. Rizzo, G. Calestani, G. Gigli, F. D. Angelis, R. Mosca, Chem. Mater. (2013) 25, 4613–4618.

45. J. Seo, S. Park, Y. C. Kim, N. J. Jeon, J. H. Noh, S. C. Yoon, S. I. Seok, Energy Environ. Sci. (2014) 7, 2642.

46. Y. Ding , X. Yao, X. Zhang, C. Wei, Y. Zhao, Journal of Power Sources (2014) 272 351.

47. J.-H. Lee, J.-J. Kim, Phys. Status Solidi A (2012) 209, 1399–1413.

48. J. Wu, J. Hou, Y. Cheng, Z. Xie, L. Wang, Semicond. Sci. Technol. (2007) 22, 824

49. J. Y. Lee, Appl. Phys. Lett. 88, 073512 (2006).

50. Y. Sun, M. Wang, X. Gong, J. H. Seo, B. B. Y. Hsu, F. Wudl, A. J. Heeger, J. Mater. Chem. (2011) 21, 1365–1367.

51. H. Gommans, B. Verreet, B. P. Rand, R. Muller, J. Poortmans, P. Heremans, J. Genoe (2008) 18, 3686–3691.

52. Q. L. Song, C. M. Li1, M. L. Wang, X. Y. Sun, X. Y. Hou, Appl. Phys. Lett. (2007) 90, 071109.

53. M. Vogel, S. Doka, C. Breyer, M. C. Lux-Steiner, K.

Fostiropoulos, Appl. Phys. Lett. (2006) 89, 163501.

54. H. J. Snaith, A. Abate, J. M. Ball, G. E. Eperon, T. Leijtens, N. K. Noel, S. D. Stranks, J. T.-W. Wang, K. Wojciechowski, W. Zhang, J. Phys. Chem. Lett. (2014) 5, 1511−1515.

55. E. L. Unger, E. T. Hoke, C. D. Bailie, W. H. Nguyen, A. R. Bowring, T. Heumüller, M. G. Christoforo, M. D. McGehee, Energy Environ. Sci. (2014) 7, 3690-3698.

56. H.-S. Kim, N.-G. Park, J. Phys. Chem. Lett. (2014) 5, 2927−2934.

57. M. Herman, M. Jankovec, Marko Topic, Int. J. Photoenergy (2012) 2012, 151452.

초 록

유기물/무기물 혼합 페로브스카이트 태양전지는 최근 높은 전력변환 효율을 보이며 매우 많은 주목을 받고 있다. 현재까지 대부분의 페로브스카이트 태양전지는 용액공정으로 제작되어왔다. 용액공정을 이용한 페로브스카이트 태양전지의 중요한 주제 중 하나는, 박막의 균일도, 작은 구멍, 수분 및 대기에의 취약성 등을 제어하기 어려움에서 오는 재현성 문제이다. 진공 증착은 박막 형성 인자들과 수분 및 용매가 없는 깨끗한 환경에서 증착이 가능하기 때문에 재현성 문제를 해결할 수 있는 가능성이 큰 방법이다. 페로브스카이트 태양전지의 또 다른 중요한 사안은 효과적인 전하 수송 층, 특히 정공 수송 층, 을 적용하여 고 효율의 소자 특성을 얻는 것이다. 가장 널리 쓰이는 정공 수송층인 2,2',7,7'-Tetrakis(N,N-di-p-methoxyphenylamine)-9,9'-spirobifluorene (spiro-OMeTAD)는 페로브스카이트의 가전자대 에너지보다 수백 meV가 높기 때문에, 최적화된 정공 수송 층이라고 볼 수 없다.

이 학위논문에서는 진공증착으로 제작 된 molybdenum oxide (MoO_3) 와 N,N′-Di(1-naphthyl)-N,N′-diphenyl-(1,1′-biphenyl)-4,4′-diamine (NPB) 층을 사용한 페로브스카이트 태양전지를 위와 같은 문제점을 해결 할 수 있는 방법으로 제시한다. 페로브스카이트 층을 포함한 모든 다른 층, 정공 수송 층, 전자 수송 층, 완충 층, 모두 진공에서 제작되었다. NPB 층 위에서 균일한 페로브스카이트 결정을 얻을 수 있었다. 결정 입도는 약 100 nm, 평균평방근 거칠기는 약 9.7 nm 를 보였다. MoO_3/NPB 층을 정공 추출 층으로 사용한 결과 개방 전압은 1.12 V로, 현재까지 보고된 수치 중에 가장 높은 수치들 중 하나인 값을 보였다. 이러한 효과적인 정공 추출 층으로 인해, 제작된 태양전지는 최고 전력 변환 효율 13.7%, 단락 전류 밀도 18.1 mA/cm^2, 개방전압 1.12 V, 충진율 0.67의 성능을 보였다.

또한 진공 증착된 페로브스카이트 태양전지의 재현성은 11.1%의 평균 전력변환 효율을 보이며 좋은 재현성을 보였다. 전류밀도와 개방전압은 17.2 mA/cm^2 ~ 19.5 mA/cm^2 각각 0.98 V ~ 1.12 V의 분포를 보이며, 평균값에서 7% 이내의 오차로 분포되어 비교적 좋은 재현성을 나타내었다. 하지만 충진율은 0.39 ~ 0.68 사이로 분포되며 상대적으로 넓은 분포를 보이며 이는

전력변환효율에도 영향을 주어 7.1%~13.7%의 분포를 보이게 되었다. 하지만 일반적인 용액공정으로 제작된 페로브스카이트 태양전지에 비해서는 여전히 높은 재현성을 보인다. 충진율의 넓은 분포의 이유는 현재 명확하지 않지만 이 이유를 밝혀내고 개선한다면 진공증착으로 더욱 좋은 재현성을 확보 할 수 있을 것이다. 진공증착된 페로브스카이트 태양전지는 이력곡선(hysteresis) 거동을 보였다. MoO_3/NPB 층을 사용한 소자는 순방향으로 측정 시 전력 변환효율 12.1%, 단락전류밀도 18.1 mA/cm^2, 개방전압 1.09 V 그리고 충진율 0.62를 보인 반면, 역방향 측정 시 전반적으로 감소된 전력 변환효율 10.3%, 단락전류밀도 17.1 mA/cm^2, 개방전압 1.07 V 그리고 충진율 0.56을 보였다. 이력곡선 거동에 대한 정확한 기원은 현재 밝혀지지 않았기 때문에, 앞으로 많은 연구가 더 필요하다.

주요어: 유기물/무기물 혼합 페로브스카이트 태양전지, 전진공공정, 재현성, MoO_3, NPB

학 번: 2012 - 20577

Awards

- **Beom-Soo Kim**, Tae-Min Kim, Min-Soo Choi, Hyun-Sub Shim and Jang-Joo Kim, “Best Poster Award”, The 6rd Asian Conference on Organic Electronics, Nov. 12-14, 2014

List of Publications

- **Beom-Soo Kim**, Tae-Min Kim, Min-Soo Choi, Hyun-Sub Shim and Jang-Joo Kim, "**Fully vacuum–processed perovskite solar cells with high open circuit voltage using MoO_3/NPB layer"** *Organic Electronics* Volume 17, February 2015, Pages 102–106.